Experimental and numerical study of a turbulent boundary layer with pressure gradients

By PHILIPPE R. SPALART[1]†
AND JONATHAN H. WATMUFF[2]‡

[1] NASA Ames Research Center, Moffett Field, CA 94035, USA
[2] NASA Stanford Center for Turbulence Research, Stanford, CA 94305, USA

The boundary layer develops along a flat plate with a Reynolds number high enough to sustain turbulence and allow accurate experimental measurements, but low enough to allow a direct numerical simulation. A favourable pressure gradient just downstream of the trip (experiment) or inflow boundary (simulation) helps the turbulence to mature without unduly increasing the Reynolds number. The pressure gradient then reverses, and the β-parameter rises from -0.3 to $+2$. The wall-pressure distribution and Reynolds number of the simulation are matched to those of the experiment, as are the gross characteristics of the boundary layer at the inflow. This information would be sufficient to calculate the flow by another method. Extensive automation of the experiment allows a large measurement grid with long samples and frequent calibration of the hot wires. The simulation relies on the recent 'fringe method' with its numerical advantages and good inflow quality. After an inflow transient good agreement is observed; the differences, of up to 13%, are discussed. Moderate deviations from the law of the wall are found in the velocity profiles of the simulation. They are fully correlated with the pressure gradient, are in fair quantitative agreement with experimental results of Nagano, Tagawa & Tsuji, and are roughly the opposite of uncorrected mixing-length-model predictions. Large deviations from wall scaling are observed for other quantities, notably for the turbulence dissipation rate. The a_1 structure parameter drops mildly in the upper layer with adverse pressure gradient.

1. Motivation, and design of the flow

The boundary layer without pressure gradient has been studied in great detail, and its lowest-level scaling laws confirmed over a wide range of its only parameter, the thickness Reynolds number (Coles 1962). We are referring to the laws proposed for the velocity profile, and probably for the shear stress. Doubts remain for the normal Reynolds stresses (Bradshaw 1967b; Perry, Henbest & Chong 1986; Spalart 1988a; Wei & Willmarth 1989; Antonia *et al.* 1992), not to mention higher turbulence moments. The distinction between 'Reynolds-number effects' and 'low-Reynolds-number effects' needs to be clarified. The much wider parameter space of flows with pressure gradient has naturally been explored in less depth. Scaling laws cannot be

---

† Present address: Boeing Commercial Airplane Group, MS 7H-96, PO Box 3707, Seattle, WA 98124-2207, USA.
‡ Present address: MCAT Institute, NASA Ames Research Center, Moffett Field, CA 94035, USA.

expected to be as simple, particularly in the upper region, and the available prediction methods leave much room for improvement.

Much of the study of pressure gradients has dealt with so-called 'equilibrium' or 'self-similar' boundary layers which are subjected to a sustained pressure gradient, adjusted with the avowed objective of duplicating the scaling law of the zero-gradient flow in the upper region, the 'defect law'. The wall region is less disturbed than the upper region, except close to separation. This concept results in a one-parameter family and represents a cautious extension of the theory away from the zero-gradient case. There is a lack of consensus as to which pressure distributions can generate a self-similar turbulent boundary layer (Clauser 1954; Coles 1956, 1957; Bradshaw 1967a), about the uniqueness of the asymptotic state of the flow in a given – especially adverse – pressure gradient (Clauser 1954; Head 1976), and about which velocity scale is appropriate in the defect law (Coles 1956; Schofield 1981 and references therein). Decisive progress in this area is necessary, but not sufficient for the creation of prediction methods accurate in most situations, which are often far from being self-similar.

Experimental results on flows with pressure gradients up to 1968 are listed by Coles & Hirst (1968). More recent studies include Jones & Launder (1972), Samuel & Joubert (1974), Frei & Thomann (1980), Simpson *et al.* (1981), Hirt & Thomann (1986), Dengel & Fernholz (1990), and Nagano, Tagawa & Tsuji (1992). Adverse gradients are of more practical interest – because of separation, of more theoretical interest – because the wall shear stress does not dominate the situation, and more delicate experimentally – because of their higher sensitivity to upstream conditions, their tendency not to remain two-dimensional in the mean, and of the higher probability for the instantaneous velocity vector to be at large angles to the mean flow direction (this degrades the accuracy of hot-wire measurements).

As a subject for direct numerical simulation (DNS), turbulent pressure-gradient flows add to the perennial obstacles of very large memory and computational time new difficulties, arising from non-trivial boundary conditions. Self-similar boundary layers were simulated first because of the convenience they afforded in a multiple-scale approximation (Spalart & Leonard 1986; Spalart 1986). The results were very satisfactory in favourable gradients, but much less so in adverse gradients. For the same pressure-gradient parameter β, the defect profile was far from agreeing with the experiment even though the shear stress did. Possible reasons were: failure of the multiple-scale approximation due to much larger growth angles; failure of the one-parameter concept of self-similar boundary layers due to the large Reynolds-number difference; and experimental errors, including in the wall-shear measurement and in the two-dimensionality.

The need to explore this discrepancy, the promise of DNS as a 'numerical experiment' with full detail of all quantities and unambiguous wall-shear evaluation, and some questions of experimental technique such as the accuracy of X-wires, led to the design and parallel study of a low-Reynolds-number adverse-pressure-gradient (APG) boundary layer. The Reynolds numbers in previous experimental studies were many times larger than can be considered for a DNS. This paper reports on the region of the flow accessible to the simulation, which is only a third of the experimental run. The experimental results in the region downstream, in which the flow approaches self-similarity, will be presented elsewhere.

The overall characteristics of the experiment were presented by Watmuff & Westphal (1989), and extensive measurements were reported by Watmuff (1990). Figure 1 is a sketch of the flow. Lengths are expressed in metres for lack of a better
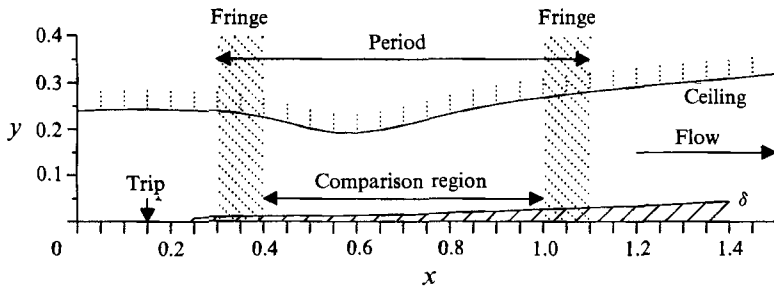
FIGURE 1. Flow configuration.

lengthscale and distance from the origin in x. The pressure coefficient C_p is based on a reference velocity U_{ref}, which is the core velocity at the inlet of the experiment $(x = 0)$. A simulation much beyond $x = 1$ was not contemplated as it would require an order of magnitude increase in expenditure, and the present simulation was barely feasible. The 'period' and 'fringes' pertain to the numerical method and are explained in §3. The pressure gradient is controlled by a contoured ceiling, in the experiment. The boundary layer is fully turbulent within the comparison region (the experimental boundary layer is tripped at $x = 0.15$, and the simulated boundary layer is also turbulent at $x = 0.4$). Its thickness δ, taken from the experiment, is shown on the figure.

The Reynolds number per metre based on U_{ref} is 4.28×10^5. Lower values would have reduced the cost of the simulation, but very low Reynolds numbers reduce the range of scales so much that they raise questions about the relevance to high-Reynolds-number flows. The lowest momentum-thickness Reynolds number R_θ is about 600, which leaves a fair margin for turbulence to be sustained. An additional requirement was to choose a sufficient dynamic pressure to allow accurate measurements of pressure differences.

The region of most interest, the APG from $x = 0.6$ on, is preceded by a favourable-pressure-gradient (FPG) region from $x = 0.2$ to 0.6 (about 35 times the local δ), following an idea of Inman & Bradshaw (1981). The goal is to let the turbulence develop and lose memory of the transition (experiment) or inflow condition (simulation) with a smaller increase of R_θ than would occur with zero pressure gradient, and seems to have been achieved. Two non-dimensional measures of the pressure gradient are $\beta \equiv \delta^*[dp/dx]/\tau_w$, where δ^* is the displacement thickness and τ_w the wall shear stress, and $K \equiv \nu[dU_\infty/dx]/U_\infty^2$ where ν is the kinematic viscosity and U_∞ the edge velocity. In the FPG they take the values $\beta \approx -0.3$ and $K \approx 1.25 \times 10^{-6}$, or about half of the values that (if sustained) would force relaminarization. One of the requests from the simulator to the experimentalists was for the FPG region to be self-similar, as discussed by Watmuff & Westphal (1989). In the meantime, an advance in the numerical technique (compared with that of Spalart 1988a) made this unnecessary. However, the presence of the FPG is still considered an advantage for physical reasons.

Inman & Bradshaw (1981) estimate that 20 boundary-layer thicknesses is a sufficient distance for turbulence to develop well (as revealed by a logarithmic layer) after the trip. Herring & Norbury's (1967) estimate of the distance needed to obtain self-similarity (equilibrium, in Clauser's sense) is also 20 thicknesses. Jones & Launder (1972) found in a sink flow that two boundary layers with different inflow thicknesses (R_θ about 340 and 390) needed about 25 thicknesses before they had the same thickness and shape factor. The present experiment has over 30 thicknesses

from the trip to $x = 0.6$. In the simulation the region $[0.4, 0.6]$, considered as the entry region, represents about 14 boundary-layer thicknesses and proves sufficient to heal the boundary layer, primarily because the flow is already turbulent and the inflow thicknesses and gross turbulence energy match well.

The β-parameter rises rather rapidly from 0 around $x = 0.63$ to about 2 at $x = 1$, the end of the comparison region, so that the boundary layer is far from being self-similar (a constant β is a necessary condition for classical self-similarity). This not so much by design as it is the result of experimental and numerical constraints.

The free-stream turbulence level in the experiment is discussed below. In the simulation, free-stream turbulence is not intentionally introduced. Fine-scale turbulence cannot be supported by the grid, which rapidly coarsens in the y-direction outside the boundary layer. Irrotational velocity fluctuations with lengthscales of the order of the distance from the wall are naturally induced by pressure forces and are of the order of 1 % of the edge velocity near the edge of the boundary layer. Small vorticity fluctuations also exist, induced by numerical errors. No attempt was made to match any of the characteristics (intensity, lengthscales) of the free-stream turbulence.

2. Experimental technique
2.1. *Wind tunnel and probe traverse*

The experiment was performed in a blower-driven open-return wind tunnel in the Fluid Mechanics Laboratory at NASA Ames Research Center. A description of the facility is given by Wood & Westphal (1988). Since then a new 5:1 two-dimensional contraction with exit dimensions of 1.0 by 0.24 m and a new working section have been installed. The layer develops on a 1.0 m wide by 2.1 m long polished aluminium plate forming the test-section floor. A flexible ceiling is contoured to produce the pressure distribution and two Plexiglas sidewalls complete the test section.

A high-speed three-dimensional computer-controlled probe traverse is integrated into the test section. The range of motion is 2.1 m in the x-, 0.1 m in the y-, and 0.5 m in the z-directions. Linear stepping motors are used for the y- and z-axes to obtain accurate (± 0.025 mm) as well as high-speed (1.5 m/s) positioning. Probes are fixed to a sting which is carried by the y-axis motor. The y-axis motor rides on a steel platen which is attached to the z-axis motor, linear bearing and platen assembly. The z-axis assembly is supported above the test wall within the working section by a gantry which spans the distance between the side-walls. The gantry is constructed of carbon-fibre composite and plates are fixed to each end which protrude through gaps left between the edges of the test plate and the side walls. Overlapping rubber strips are used to seal the gaps. The end plates are attached to carriages located beneath the test-plate which move on linear bearings in the x-direction. A brushless linear d.c. motor is attached to one of the x-axis carriages for streamwise positioning. The motor reacts with a long magnet track to provide a maximum propulsive force of 350 N. The motor is operated as a closed-loop servo system with feedback provided by a linear quadrature encoder with a resolution of 10 µm. The friction introduced by the rubber seals and the linear bearings limit the positional accuracy to ± 0.1 mm. By *itself* the gantry weighs only about 2 kg which is only 10% of the total movable mass. Loading the gantry with a 10 kg weight in the centre of its 1 m span results in a deflection of only 0.05 mm, showing that it is very stiff.

Locating the traverse hardware for the y- and z-axes within the test section is the most convenient way of implementing the three-dimensional capability. The

projected area in the streamwise direction of all the apparatus located within the tunnel is equivalent to a 30 mm-thick object spanning the tunnel sidewalls, so the blockage is not excessive. Nevertheless the traverse presents a severe disturbance in the downstream flow and preliminary measurements were performed both with and without the traverse in the working section in order to estimate its upstream influence. As a result of these observations probe tips are located 0.4 m upstream of the gantry, which is about twice the maximum distance for which the disturbances could be detected during these tests.

The three-dimensional capability offers several advantages compared to a more conventional arrangement. For example, hot-wire probes must be calibrated frequently in a uniform stream. If a more conventional single-axis traversing system were used in this experiment then the probes would have to be transferred manually back and forth between the calibration region and measurement stations. This would consume valuable time as well as introducing the risk of breaking the fragile and expensive probes. With the computer-controlled three-dimensional traverse this operation can be performed in a matter of seconds with minimal risk of probe damage. Additionally, the traverse acts as a shaker for imposing accurately known velocity perturbations on the cross-wire probes for calibration purposes as described in §2.5.2. Other benefits of the traversing system are described in §2.6. Finally, it is worth noting that the streamwise speed of the traverse has been tested at 2 m/s which is sufficient for 'flying hot-wire' measurements in regions of high turbulence intensity (see Watmuff, Perry & Chong 1983). However, it has not been necessary to exploit this feature in this experiment.

2.2. *Selection of a transition device*

The boundary layer on the test plate has its origin upstream and is influenced by the pressure gradients and wall curvature within the contraction. The low-Reynolds-number requirement of this experiment makes the quality of the incoming laminar boundary layer more important than usual. Laminar boundary layers are especially sensitive to adverse pressure gradients and are prone to separate, causing increased unsteadiness. Laminar boundary-layer profiles were measured with a Pitot tube at $x = 0.083$ for a number of free-stream velocities ranging from 6 to 12 m/s. The pressure gradient was zero along the entire test section for these measurements. All the profiles were found to be very close to the Blasius profile. In particular the boundary layer corresponding to $U_{ref} \approx 6.5$ m/s used in the experiment had a shape factor $H = 2.45$, close to that of the Blasius profile, $H = 2.59$.

The low-Reynolds-number requirement also means that measurements are needed close to the tripping device. The effect of a simple cylindrical wire has been the subject of many studies, see Schlichting (1979, p. 537) for a review. More recently there have been observations of spanwise irregularities in the boundary layers behind trip wires and many workers have suggested that distributed three-dimensional roughness elements may be superior for transition purposes. However, we are not aware of a systematic parametric study that offers a reproducible alternative to a trip wire. The observed irregularities have varying strengths depending on the facility. There is evidence to suggest (see Bradshaw 1965) that the observations are more closely coupled with wind-tunnel screens than with trip wires.

For the reasons outlined above a cylindrical wire was selected to bring about boundary-layer transition. The diameter and streamwise position for a number of wires were determined using the guidelines reported by Schlichting in conjunction with the laminar velocity profiles. Boundary-layer profiles were measured behind the

trip wires in a zero pressure gradient. Satisfactory results were obtained with 1.7 mm and 2.0 mm (diameter) wires positioned near the contraction exit. However at a location 0.15 m downstream of the contraction the 1.7 mm wire failed to produce transition at all, while the 2.0 mm wire produced intermittent transition. This is probably due to the adverse pressure gradient (not measured) near the exit of the contraction. Reliable transition was obtained with a 2.4 mm diameter wire at $x = 0.15$ m. Measurements of C_f, θ and H indicated that a 'normal' boundary layer was established behind the 2.4 mm wire by $x = 0.35$ m (approximately 20δ downstream of the wire) corresponding to $Re_\theta \approx 500$.

As mentioned previously, the reference velocity U_{ref} at the entrance to the test section is around 6.5 m/s, corresponding to the reference unit Reynolds number of 4.28×10^5 m^{-1} which is maintained constant to within $\pm 1\%$ during all measurements. The free-stream turbulence intensity in the test section near the exit of the contraction is 0.2 %.

2.3. *Mean-flow two-dimensionality*

Spanwise surveys of C_f were conducted at 5 mm intervals in the z-direction and at 50 mm intervals in the x-direction. At $x = 0.4$ the spanwise variation of C_f is within $\pm 1.5\%$ over 28δ; at $x = 0.6$, $\pm 1.2\%$ over 24δ; at $x = 0.8$, $\pm 1.8\%$ over 17δ; and at $x = 1.0$, $\pm 3.1\%$ over 12δ. Figure 6 shows that the streamwise momentum balance of the experimental data is satisfactory. These results indicate that the layer is acceptably two-dimensional.

2.4. *Pressure and skin-friction measurements*

The pressure differences in the test section are measured using a MKS Baratron 398H differential pressure transducer with a range of 133 Pa and a 270B signal conditioner. A Pitot-static tube located near the exit of the contraction is used for the reference total and static pressures. The static pressure is used as the reference pressure for the transducer. A traversing Pitot tube, 44 static wall pressure tappings, and the reference total and static pressures are connected to the transducer via a 48-port Scanivalve pressure switch under computer control. A pause of 5 s after the connection allows the pressures to stabilize before reading the transducer and all averages are obtained over at least 90 s. Transducer drift was also non-existent. However, as a precaution, the reading obtained by connecting the same static reference pressure across the transducer was always subtracted from each measurement.

It is well known that Pitot tubes suffer from wall-proximity effects and a variety of correction schemes exist. However, it is uncertain which is the most appropriate for boundary layers. Local static pressures have not been measured away from the test surface and the Pitot tube data are reduced using the static pressure at the wall. The local static pressure throughout the layer will differ slightly from the wall static pressure owing to mean streamline curvature. Also, the Pitot-tube mean-flow data show some scatter, especially in the near-wall region, because of the small pressure differences. For these reasons the normal hot-wire mean flow data are presented instead of the Pitot tube data.

The experimental C_p variation shown in figure 2 below acts as a data base for inferring the local static wall pressure for all pressure-probe measurements. The C_p data base was created by averaging the results of a number of runs performed several months apart. There is no discernible trend in the data taken at the different times. During each run 15 separate measurement cycles of the local static pressure, and

reference total and static pressures were performed in succession and averaged to produce the resultant C_p. Using these rather long total averaging periods of around 20 min for each C_p produced an extremely smooth distribution.

The distribution of the skin friction coefficient C_f along the tunnel centreline was measured with nine Preston tubes ranging in diameter from 1.5 to 7.9 mm. The pressure difference between the Preston tube and the local static pressure ΔP can be very small owing to the low velocities in the test section. Further, ΔP is obtained by subtraction of two relatively large numbers. Therefore long time-averaging periods were necessary to obtain smooth results. Fifteen separate measurement cycles of the Preston tube pressure, and reference total and static pressures were performed in succession for each tube at each x-position. The C_f was calculated from the averaged pressures using the calibration of Patel (1965). Towards the end of the APG region ΔP can be as small as 1.5 Pa. Therefore errors of 1 % in the reference total pressure (≈ 25 Pa) or in the C_p data base lead to errors of $\approx 15\%$ in ΔP. In the FPG the larger-diameter tubes protrude into the upper region, where the mean flow deviates from the law of the wall. Consequently the C_f estimates from each of the nine tubes have been averaged using the selection criteria that the non-dimensional diameter $d^+ < 100$ and that $\Delta P > 2.5$ Pa.

The accuracy of C_f measurements by Preston tubes needs to be scrutinized since the pressure gradient parameter $p^+ \equiv \nu/(\rho u_\tau^3)\, \mathrm{d}P/\mathrm{d}x$ exceeds the limits suggested by Patel (1965) in both the FPG and APG regions. McDonald (1968) used empirical information and similarity arguments for the mixing length to estimate the effect of pressure gradients on the law of the wall. Deviations from the law of the wall were expressed in terms of p^+. In our flow $-0.009 < p^+ < 0.02$ and his results indicate deviations from the law of the wall as high as 8 %. However, for a sink flow his predictions indicate a negative deviation, in sharp disagreement with both the experiments of Jones & Launder (1972) and the numerical simulations of Spalart (1986). Therefore the accuracy of McDonald's predictions seems questionable. Frei & Thomann (1980) compared the wall shear stress τ_{w} measured directly with a floating element to values inferred from Preston tubes in axisymmetric boundary layers. Using dimensional arguments, they extended Preston's original relation, i.e.

$$\tau_{\mathrm{w}}\frac{d^2}{4\rho\nu^2} = F\left(\Delta P\frac{d^2}{4\rho\nu^2}, \frac{\mathrm{d}P}{\mathrm{d}x}\frac{\nu}{\rho u_\tau^3}, \frac{\mathrm{d}^2P}{\mathrm{d}x^2}\frac{\nu^2}{\rho u_\tau^4}, \cdots \frac{\theta}{d}\right). \tag{1}$$

Frei & Thomann suggested that upstream-history effects could be accounted for by considering only the first derivative of the pressure distribution, $\mathrm{d}P/\mathrm{d}x$. They offered an empirical correction scheme for the zero pressure gradient calibration based on results using two pressure distributions in which the second derivatives were positive and negative respectively. The correction scheme worked equally well in both cases. For the range of d^+ and p^+ in this experiment their scheme indicates that the errors are less than 3 %. However, in subsequent work Hirt & Thomann (1986) subjected boundary layers to sudden application and removal of adverse pressure gradients thus pushing the layers far from equilibrium. Preston-tube errors of up to 10 % were observed. They found that the relationship suggested by Frei & Thomann was not as general as expected and unfortunately no parameters could be found to correlate the errors, so that it is difficult to apply these more recent results to our flow.

The results from the nine Preston tubes cover the range $20 < d^+ < 100$ and the C_f are within $\pm 3\%$. Following the observations of Hirt & Thomann and Frei & Thomann, the C_f variation might be expected to follow a trend with tube diameter. However the C_f variation appears uncorrelated with d^+. Moreover, the experimental

mean velocity profiles follow both the sublayer profile and the logarithmic law fairly closely. The most significant differences appear in the FPG region where there are deviations from both the sublayer profile and the logarithmic law. This question will be discussed in depth in §4, with the help of the numerical results.

2.5. *Hot-wire measurements*

2.5.1. *Hot-wire probes*

Modified Dantec 55P05 normal and 55P51 cross-wire probes are used for the turbulence measurements. The prong separation is reduced and the prongs are stiffened with the addition of a small web. Wollastan wire is soldered to the prongs and etched to produce filaments 2.5 μm in diameter and 0.5 mm in length ($7.5 < l^+ < 13$). The distance between the cross-wire filaments is 0.2 mm. The same normal and cross-wire probes and wires have been used for all the measurements.

Perry, Lim & Henbest (1987) found substantial differences between profiles of the Reynolds shear stress $\overline{uv}$ measured in a rough-wall boundary layer where the turbulence intensities are large compared to the mean velocity. The differences in $\overline{uv}$ were found to depend on the included angle between the cross-wire filaments and on whether the probe was stationary or 'flying' upstream. The differences between the stationary and flying results were substantial for conventional probes where the included angle is nominally 90°. Only small differences were observed when the included angle was increased to 120°. By tilting the probes in a uniform stream Perry *et al.* found that a flow angle of 45° could be imposed on the probe with the 120° included angle without appreciable error, whereas the probe with 90° included angle started to show errors at flow angles as low as 20°.

Since quite high relative turbulence intensities are experienced in the APG region, the included angle between the cross-wire filament is set to 110° which is about the maximum possible angle considering the probe geometry. The axis of the cross-wire probe is tilted at an angle of 4° towards the test plate in order to obtain measurements close to the wall. Therefore the angles between the normal of each wire and the streamwise direction are 39° and 31° respectively. Histogram estimates of the probability density function of the instantaneous flow angle θ relative to V have been measured at various x- and y-positions in the layer and $\Pr[-20° < \theta < 20°] > 0.995$ in the most strongly turbulent regions. Therefore the errors described by Perry *et al.* should be insignificant.

Wall distances are set using the electrical contact of a needle with the test plate. The wall distance is calibrated by focusing a telescope on the filaments and their images in the wall. The telescope is also used to ensure accurate alignment of the filaments with respect to the wall. When the cross-wire probe is aligned normal to the wall (i.e. for U- and V-measurements) the wall distance is taken to be between the wall and the point where the filaments appear to cross when viewed from the side. When the cross-wire probe is aligned for U and W measurements the distance is taken to be between the wall and the midpoint of the filaments. The closest data point to the wall is 0.2 mm for the normal wire, and 1.2 mm for cross-wires.

2.5.2. *Hot-wire calibration and data reduction*

The wires were operated with Dantec 55M10 constant-temperature hot-wire anemometers at a nominal resistance ratio of 1.8. The anemometers were operated with a flat response for the feedback amplifier and the system response of 75 kHz is more than adequate for the measurements. A d.c. voltage is subtracted from the anemometer outputs and the resulting signals are amplified so that they lie between

± 10 V over the range of velocities to be experienced by the wires. The signals are not filtered.

The hot-wire signals are acquired and processed in real time using a high-speed 15-bit Tustin X-1500 analog-to-digital converter (ADC) and a microVAX II computer. Two arrays are set aside in computer memory and double-buffered data acquisition is used to process the data in one array while data are being acquired in the alternate array. The ADC contains a 16K hardware buffer which is connected to the computer's high-speed digital interface. While processing previously acquired data, there are clock cycles when the CPU does not need to access memory and control of the bus can be relinquished temporarily. The interface can use these clock cycles for data transfers using a Direct Memory Access technique outside of program control. Hence there is a high degree of true parallelism between data acquisition and data processing.

A more complete description of the real-time data acquisition and processing techniques is given by Watmuff (1992) in addition to the cross-wire calibration and data reduction algorithm described below. The method assumes an unmodified cosine cooling law, i.e. the component of the velocity vector along the wire is assumed to make no contribution to the heat transfer. The effective cooling velocity of each wire can be expressed as functions $f_1(E_1)$ and $f_2(E_2)$ of the amplified outputs E_1 and E_2, i.e.

$$\begin{pmatrix} f_1 \\ f_2 \end{pmatrix} = \begin{pmatrix} \cos\psi_{e1}\sin\psi_{e1} \\ \cos\psi_{e2}\sin\psi_{e2} \end{pmatrix} \begin{pmatrix} U \\ V \end{pmatrix}, \tag{2}$$

where U is the velocity component in the streamwise direction, V is the velocity component perpendicular to the streamwise direction and in the plane of the prongs, and ψ_{e1} and ψ_{e2} are the effective angles that the normals to each wire make with the streamwise direction. The difference between the effective angle and the actual wire angle compensates for not accounting for the longitudinal cooling velocity. Watmuff (1992) used a simulation to show that the compensation introduced by using effective wire angles leads to a calibration in which the errors are small for moderately large flow angles. For example, the errors $(U_o - U_i)/U_i \approx 2\%$ and $(V_o - V_i)/U_i \approx 0.5\%$ for typical wires when the out-of-plane velocity component is zero and the flow angle is 25°. (The subscript i refers to velocities imposed on the wires, while subscript o refers to output velocities as calculated from the calibration.)

A more convenient formulation of (2) is given by

$$\begin{pmatrix} g_1 \\ g_2 \end{pmatrix} = \begin{pmatrix} 1 & \tan\psi_{e1} \\ 1 & \tan\psi_{e2} \end{pmatrix} \begin{pmatrix} U \\ V \end{pmatrix}, \tag{3}$$

where $g_1(E_1) = f_1(E_1)/\tan\psi_{e1}$ and $g_2(E_2) = f_2(E_2)/\tan\psi_{e2}$. One advantage is that $g_1(E_1)$ and $g_2(E_2)$ can be determined by a simple static calibration (where it is assumed that $V = W = 0$). It is common practice to estimate ψ_{e1} and ψ_{e2} by tilting the wires in a uniform stream. However, in this experiment $\tan\psi_{e1}$ and $\tan\psi_{e2}$ are estimated by using the traverse to impose known values of V (or W) on the probe while holding U constant. A voltage proportional to motor speed is derived from the motor step pulses. The V (or W) perturbation is imposed by oscillating the probe in the y-direction (or z-direction) and the wire voltages and the motor speed voltage are sampled on the basis of the position of the motor and averaged over 50 cycles. The magnitude of the effective wire angles could be evaluated using r.m.s. quantities. However, the values of $\tan\psi_{e1}$ and $\tan\psi_{e2}$ are obtained from a linear least-squares fit applied to the perturbations of $g_1(E_1)$ and $g_2(E_2)$ as functions of the motor velocity.

The advantage of this method is that the sign is obtained in addition to the magnitude. The assumption of simple cosine cooling is vital for the high-speed data reduction algorithm because the calibration inversion is then linear with respect to $g_1(E_1)$ and $g_2(E_2)$, i.e.

$$\begin{pmatrix} U \\ V \end{pmatrix} = \begin{pmatrix} C_{U_1} & C_{U_2} \\ C_{V_1} & C_{V_2} \end{pmatrix} \begin{pmatrix} g_1 \\ g_2 \end{pmatrix},$$ (4)

where $C_{U_1} = \tan\psi_{e2}/\Delta t,$ $C_{U_2} = \tan\psi_{e1}/\Delta t,$ $C_{V_1} = -1/\Delta t,$ $C_{V_2} = 1/\Delta t$ and $\Delta t = \tan\psi_{e2} - \tan\psi_{e1}.$

Look-up tables (LUTs) are commonly used in real-time data acquisition/ processing applications when the transducer calibration is nonlinear. Using an LUT decreases the data processing time since the nonlinear calibration inversion calculations have to be performed only once for the storage. Linear interpolation schemes are generally used in conjunction with LUT arrays since the number of array elements can be minimized (within the constraints of linearity). However, the advantage of reduced memory requirements is offset by the computational overhead required for the interpolation and this serves to reduce the overall throughput. The interpolation can be avoided if the number of LUT array elements corresponds to the measurement resolution exactly over the full range. For example, if the transducer voltage is measured with a 15-bit ADC, then the LUT array of maximum density would consist of 32768 (2^{15}) words. In this case the calibration inversion can be stored for every possible value returned by the ADC and no interpolation is required. Further, the ADC word can be used directly as the index of the LUT array.

LUTs of maximum density are practical when the calibration can be expressed in terms of a single variable, such as velocity for a normal hot-wire probe, since the LUT is one-dimensional. However, a cross-wire calibration is bivariate and two-dimensional LUTs must be used if there are any terms containing cross-products of E_1 and E_2. It is impractical to use two-dimensional LUTs of maximum density owing to the excessively large memory requirements. Each LUT array would need to consist of 2^{30} elements when using the 15-bit ADC mentioned above, so that the total size of the LUT arrays would have to be 8 Mbytes to avoid interpolation (allowing 4 bytes per element). The calibration scheme given by (4) does not contain cross-product terms so that it is practical to use a pair of one-dimensional LUTs of maximum density and linear interpolation can be avoided. This is the fastest possible method for evaluation of the functions $g_1(E_1)$ and $g_2(E_2)$.

It should be emphasized that the nonlinearity of the calibration is incorporated into the LUTs and that once $g_1(E_1)$ and $g_2(E_2)$ are known, the remaining calibration inversion calculations are linear. It is this linearity that allows an algorithm to be devised for the calculation of the mean flow and Reynolds stress components that does not require the LUT values of $g_1(E_1)$ and $g_2(E_2)$ to be converted to U and V for every sample of E_1 and E_2. Only running totals of $g_1(E_1)$ and $g_2(E_2)$ and their squares and cross-product need to be evaluated for final averaging. The mean flow and Reynolds stress components can all be calculated from the final averages using

$$\begin{pmatrix} \overline{U} \\ \overline{V} \end{pmatrix} = \begin{pmatrix} C_{U_1} & C_{U_2} \\ C_{V_1} & C_{V_2} \end{pmatrix} \begin{pmatrix} \overline{g_1} \\ \overline{g_2} \end{pmatrix}$$ (5)

and

$$\begin{pmatrix} \overline{u^2} \\ \overline{uv} \\ \overline{v^2} \end{pmatrix} = \begin{pmatrix} C_{U_1}^2 & 2C_{U_1}C_{U_2} & C_{U_2}^2 \\ C_{U_1}C_{V_1} & (C_{U_1}C_{V_2}+C_{U_2}C_{V_1}) & C_{U_2}C_{V_2} \\ C_{V_1}^2 & 2C_{V_1}C_{V_2} & C_{V_2}^2 \end{pmatrix} \begin{pmatrix} \overline{g_1^2} - (\overline{g_1})^2 \\ \overline{g_1 g_2} - (\overline{g_1})(\overline{g_2}) \\ \overline{g_2^2} - (\overline{g_2})^2 \end{pmatrix}$$ (6)

Avoiding the conversion to U and V reduces the number of floating point calculations N_f required for each pair of samples from $N_f = 14$ (7 multiplications and 7 additions) to $N_f = 8$ (3 multiplications and 5 additions), i.e. the number of floating point calculations is nearly halved. Watmuff (1992) has extended the algorithm for the determination of triple products such as $\overline{u^2v}$.

As mentioned previously, Watmuff (1992) used a simulation to examine the errors in discrete realizations of U and V introduced by the assumption of simple cosine cooling. In an effort to explore the errors introduced in turbulence quantities he also performed a Monte Carlo simulation by generating a pseudo-random time series of (U, V, W) with a covariance matrix representative of turbulent flows. The simulation examined the effect of high turbulence levels, both with and without a w' component, for both a 'perfect' calibration and a calibration based on the algorithm described above. The errors in the mean flow and turbulence quantities were less than 1% when $w' = 0$ for both calibrations, even for relatively high turbulence intensities e.g. $u_{\mathrm{rms}} = 20\%$. However, the errors introduced by w' were significant for all quantities using both calibrations, with the exception of $\overline{v^2}$ in the case where longitudinal cooling was accounted for. The results of the simulation suggest that the errors in $\overline{uv}$, $\overline{v^2}$ and $\overline{w^2}$ due to the out-of-plane velocity component are of similar magnitude and could reach values as large as -5% to -10% in the most highly turbulent regions (i.e. near the wall towards the end of the FPG). No attempt was made to correct the cross-wire data for w' fluctuations.

The wires are calibrated against the reference Pitot-static tube in the zero-pressure-gradient region at $x = 0.1$ m. Ten operating points are used over the range of velocities to be experienced by the wires. By repeating hot-wire measurements at the same position it was discovered that the most consistent data in the near-wall region are obtained if the zero-velocity operating point is included in the calibration. The condition when the tunnel fan become stationary is determined by monitoring short-term averaged hot-wire voltages as the flow slows down. Hot wires are very sensitive at zero velocity and small background draughts can cause large voltage fluctuations. However, there is evidence to suggest that flow reversals occur in this situation, i.e. the velocity time history does contain points of exactly zero velocity at which point the hot-wire signals are subject to rectification. The operating point corresponding to zero velocity is taken to be the minimum voltage observed during a 30 s period after the tunnel fan becomes stationary. No attempt is made to account for the effects of natural convection. Third-order least-squares polynomial fits to the calibration data are used to generate LUTs for the functions $g_1(E_1)$ and $g_2(E_2)$. By carefully tuning various parameters such as the sampling rate and sample size, the combination of the double-buffered data acquisition/processing scheme and the new cross-wire data reduction algorithm provides a maximum on-line mean-flow and Reynolds-stress evaluation rate of 10k samples/s, even though bounds checking is used for the LUT arrays and the running totals are evaluated in double precision. Moreover, this data reduction rate can be sustained indefinitely so that an arbitrarily large number of samples can be processed. A similar calibration and data-processing scheme is used for the normal wires. However, the data reduction is much simpler since the LUT returns the streamwise velocity directly. The decreased computational overhead means that the maximum normal-wire data reduction rate is 25k samples/s.

In the FPG region the sampling rate was typically 7.5 kHz and 10 sets of 30k samples were found to produce adequate data convergence at each data point. In the

APG the sampling rate was reduced and more samples were required to achieve a similar degree of smoothness in the data.

2.6. *Automation of the experiment*

Total computer control of tunnel speed, probe traversal and data acquisition has allowed all experimental procedures to be automated. Sophisticated software enables long-duration experiments to be performed continuously over several days without manual intervention. This mode of operation required several significant new developments. For example, large and complex three-dimensional measurement grids can be programmed and viewed ahead of time. Hot-wire calibration drift is monitored and new calibrations are performed (automatically) if the drift exceeds some tolerance. Other features that have proved vital for long-duration unattended experimental runs include automatic error-detection/recovery schemes and the provision of 'emergency' asynchronous manually initiated software interrupts for hardware checkouts and to provide access to approximately 125 menu-settable control variables.

Automation of the experiment allows massive quantities of data to be processed on-line over a relatively short period. Spatially dense mean-flow and Reynolds-stress profiles have been measured along the tunnel centreline at 50 mm intervals from $x = 0.2$ to 2.0 m, i.e. 37 profiles. The close spacing of the profiles is needed in the region of FPG to examine the recovery from upstream trip effects and the approach to self-similarity and in the region of APG where there is rapid growth with streamwise distance. The spacing of the profiles also provides a sensitive means for detecting anomalous data. The data downstream of $x = 1.0$ m indicate that the flow approaches self-similarity. These results will be presented elsewhere.

The greatest obstacle in obtaining high-quality data has been hot-wire calibration drift caused by large changes in ambient temperature. Variations of up to 15 °C are typical over a 24-hour period while changes of up to 3 °C have been observed over a period as short as 5 minutes. Automation of the experiment has provided a solution to this thorny problem, i.e. hot-wire profiles are repeated until the drift check obtained after a profile is measured is within a certain tolerance of a drift reference taken immediately after the wires have been calibrated. Setting the drift tolerance at 0.5% (larger tolerances introduce too much scatter in the data) has meant that on average a profile must be measured 5 times before it is acceptable. At the time of writing over 1000 normal- and cross-wire profiles have been measured.

3. Numerical technique

3.1. *Presentation of the fringe method*

This work involves a new application of an established numerical method (Spalart, Moser & Rogers 1991). It solves the incompressible Navier–Stokes equations over a flat plate, at $y = 0$, with periodic conditions in the x- and z-directions, parallel to the plate. The spatial discretization is spectral, making use of Fourier series in x and z and Jacobi polynomials matched to an exponential mapping in y. The temporal discretization is by a hybrid second-order-accurate finite-difference scheme (Spalart *et al.* 1991).

Usually, periodic conditions can be used only if the turbulence is statistically homogeneous in the direction considered, and boundary layers are almost never homogeneous in the x-direction. In the past this conflict was addressed by

considering flows that are only slightly inhomogeneous in x, and introducing a multiple-scale approximation. This led to a mathematical problem that was homogeneous in x, and whose solution was closely related to that of the true spatially evolving problem at a given station X (Spalart 1986, 1988a). This modified problem consisted of the Navier–Stokes equations, with the addition of small 'growth terms'. This strategy was successful in the sink flow, with a sustained FPG, and in the flow with zero pressure gradient. If the pressure gradient is applied suddenly and/or is strong and adverse, the assumption of slight inhomogeneity fails. In addition, the multiple-scale method was somewhat crude, and algorithmic constraints prevented the inclusion of one of the growth terms (Spalart 1988a). There has been no evidence – either poor comparison with experiment or lack of internal consistency – that the growth-term approximation compromised the solutions. Nevertheless, it introduced an uncertainty into the method, which was more significant in the upper part of the boundary layer.

These considerations and the desire to treat more strongly inhomogeneous flows led to a new approach. As an example, we are conducting the simulation of a small separation bubble with the new method (Coleman & Spalart 1993), which would be impossible with the growth-term approach. Periodic conditions are still applied and extra terms added to the equations (because of the decay of momentum and kinetic energy, this is unavoidable if a statistically steady state is to be obtained). However, within the period in x we distinguish a 'fringe region' in which the extra terms are finite, and a 'useful region' in which they are zero and therefore the Navier–Stokes equations apply. See figure 1. Instead of growth terms that were small, derived from an approximation, and active over the whole domain, we have extra terms that are finite and arbitrary, but confined to the fringe. Only the results in the useful region will be compared to the experimental data. Issues of credibility now arise only at the interfaces between fringe and useful region. These interfaces act as an inflow and outflow boundary for the useful region (fluid particles travel through the useful region, then the fringe, then again the useful region). Naturally there are other vehicles of information such as pressure signals. Note that credibility at the outflow and especially at the inflow must be established in any inflow–outflow situation, whether numerical or experimental. This is discussed in §3.5.

3.2. *Implementation*

We divide the velocity field U into $U_0 + U_1 + U_2 + U_3$, where U_1 is the unknown, U_0 and U_2 are prescribed, and U_3 is a correction that depends weakly on U_1. The role of U_0 is to input the desired slip velocity for the flow over the boundary layer, and therefore indirectly the mean pressure gradient, while satisfying the no-slip condition at the wall. We define the 'slip velocity' as the extrapolation across the boundary layer, down to $y = 0$, of the velocity in the irrotational region. The notion of 'edge velocity' that is so familiar in boundary layers is hardly useful in a Navier–Stokes calculation with pressure gradients because in the free stream the velocity satisfies $U_{xx} + U_{yy} = 0$; in general U_{xx} and therefore U_{yy} are not zero, thus preventing U from approaching a constant as $y \to \infty$. In addition, in a DNS, imposing the average velocity given by the experiment as a boundary condition at or even near the edge of the boundary layer would be incorrect, since there are turbulent fluctuations there. Such a boundary condition would at the least need to be compliant in some manner. These factors account for the seemingly contrived manner in which the free-stream 'boundary condition' is applied here.

Assume that a 'target' slip velocity distribution $U_{0w}(x)$ is given over the interval

$[x_0, x_0 + \Lambda_x]$ and is periodic, and let $\hat{U}_{0\mathrm{w}}(k)$ be its Fourier transform. The Fourier transform $\hat{U}_0(k, y)$ of $U_0(x, y)$ is then prescribed as follows:

$$\hat{u}_0(k, y) = \hat{U}_{0\mathrm{w}}(k) \left[\cosh\left(k[y - y_2]\right) - \cosh\left(ky_2\right)\exp\left(-y/y_3\right)\right], \qquad (7a)$$

$$\hat{v}_0(k, y) = -\mathrm{i}\hat{U}_{0\mathrm{w}}(k) \left[\sinh\left(k[y - y_2]\right) - \sinh\left(ky_2\right)\exp\left(-y/y_3\right)\right], \qquad (7b)$$

where $y_3 \equiv \tanh(ky_2)/k$. The variables $\hat{U}_3$ and $\hat{U}_{3\mathrm{w}}$ will be related by the same formula. The U_0 field satisfies the no-slip condition, is divergence free, and is irrotational except close to the wall, within a region of thickness a few times y_2. Formulae somewhat different from (7) can satisfy these requirements, and have been used. The lengthscale y_2 is chosen to be about $\frac{1}{5}$ of the minimum expected boundary-layer thickness $\delta_{\min}$ (so that U_0 is essentially irrotational outside the boundary layer) and is not critical since altering y_2 within reasonable limits merely transfers part of the velocity field from U_0 to U_1. U_0 contains only long waves, so that $ky_2 \ll 1$ and y_3 is close to y_2.

Note that U_0 is unbounded as $y \to \infty$. This does not cause problems because the quantity that enters the momentum equation, in rotational form (which we use, see Spalart *et al.* 1991), is $U \times \omega$ and the vorticity ω is very small outside the boundary layer. In the worst case, ω decays at the rate $\exp(-y/y_0)$, where y_0 is the mapping parameter and is here 0.012, and U_0 grows like $\exp(ky)$. The largest k involved in U_0 here is 10π, so that the integral of $U_0 \times \omega$ converges. In addition, the elevation of the highest grid point of the numerical method is not large compared with Λ_x, and $\hat{U}_{0\mathrm{w}}(k)$ is sizeable only for the first few values of k (because $U_{0\mathrm{w}}(x)$ is smooth). As a result, quantities such as $\sinh(ky)$ do not take values larger than about 12 in the present simulation.

We recognize that the unbounded growth of U_0 as given by (7) would cause serious problems in a numerical method that is not in rotational form, and formally extends to ∞ in y. It may seem as if the fringe method is dependent on some aspects of our numerical method, which would reduce its general value. This assessment would be too negative, because there is no conflict between the fringe method and the use of a truncated domain in y. The core of the difficulty is that generating the inviscid flow over the boundary layer amounts to finding a stream function Ψ that satisfies Laplace's equation, with both Ψ and Ψ_y prescribed at $y = 0$. Whether using periodicity or conventional inflow and outflow conditions, this problem is ill-posed for short waves, and its solutions diverge as $y \to \infty$. Therefore truncation seems quite viable, and unless the truncation height is much lower than the height of the ceiling in the experiment, it is as justified as our approach with an infinite domain.

The role of the extra term U_2 is to process the boundary layer in the fringe, so that it has the desired thickness when it re-enters the useful region. This is done by giving U_2 a component $v_2 < 0$, towards the plate. We could have suction through the plate, but this causes numerical difficulties because of the non-zero v-component at the wall, where the grid is very fine. We also wish to disturb the wall layer as little as possible. It is therefore advantageous to forsake the continuity condition in the fringe, and to give U_2 a negative divergence. Accordingly, u_2 is 0 and v_2 is given by

$$v_2(x, y) = -Sy[1 - \exp(-y/y_1)]\, G(x), \qquad (8a)$$

$$G(x) = \left\{ \exp\left(-\left[\frac{x - x_0}{x_1}\right]^2\right) + \exp\left(-\left[\frac{x - x_0 - \Lambda_x}{x_1}\right]^2\right) \right\}, \qquad (8b)$$

where S, x_1, and y_1 are parameters. The peak value of $|v_2|$ at the edge of the boundary layer (reached at the periodic seam $x = x_0$ or $x_0 + \Lambda_x$, where $G = 1$) is typically 25%

of the free-stream velocity. The quantity $S\delta x_1/(U_\infty \varLambda_x)$ (with δ an average of the outflow and inflow thicknesses) needs to be about 0.013 in order to reverse the entrainment of non-turbulent fluid. A fair value for y_1 is $U_\infty/[3\,\mathrm{d}U/\mathrm{d}y]$ where both the edge velocity and the slope are taken at the inflow, and the slope at the wall. Usually x_1 and y_1 are chosen once and for all, and S is adjusted manually to obtain the desired inflow thickness. Low values of S will fail to sufficiently thin the boundary layer. Very high values may cause numerical problems (revealed by oscillations and spurious vorticity in the free-stream) as the method is unable to resolve an extremely thin boundary layer, not to mention quenching the turbulence. The x-dependence ($8b$) consists of a half-Gaussian at each end of the period. Since the Gaussian has fallen by more than two orders of magnitude when its argument reaches about 2.5, the useful region (defined as the region where v_2 is negligible) is roughly $[x_0+2.5x_1, x_0+\varLambda_x-2.5x_1]$.

Having chosen U_0 and U_2, and pending the definition of $U_{3\mathrm{w}}(k)$, we solve for U_1. It satisfies the divergence-free condition $\nabla \cdot U_1 = 0$ and homogeneous boundary conditions, $U_1(x,0,z) = 0$ and $U_1 \to 0$ as $y \to \infty$. The momentum equation is

$$\partial U_1/\partial t = (U_0 + U_1 + U_2 + U_3)$$
$$\times (\omega_0 + \omega_1 + \omega_3) - \nabla P + \nu\nabla^2(U_0 + U_1 + U_3) - S'G(x)\,g(y)\,U', \quad (9)$$

where S' is a parameter currently equal to $\frac{1}{2}S$, $g(y) = \exp(-[y/0.007]^2)$, and U' is the deviation of U from its spanwise (z) average. The need for this last term will be discussed shortly. P is the total-pressure field ($P \equiv p + \frac{1}{2}|U|^2$). It is periodic in x and z, and adjusts itself so that $\nabla \cdot U_1 = 0$ is satisfied. In the useful region $G(x)$ is essentially zero, and (9) is the Navier–Stokes equation for $U = U_0 + U_1 + U_3$. In earlier applications, U_0 was itself a (laminar) Navier–Stokes solution which simplified (9) (Spalart 1988b). However, adding $U_0 + U_2 + U_3$, $\omega_0 + \omega_3$, $\nu\nabla^2(U_0 + U_3)$, and the S' term to a Navier–Stokes solver written for U_1 is straightforward, using the explicit part of the time-integration scheme.

In the fringe, the Navier–Stokes equations are violated for two reasons: $\nabla \cdot U = \nabla \cdot U_2 < 0$, which is essential to reduce the thickness; ω_2 and $\nu\nabla^2 U_2$ are omitted, which is not essential but has the numerical advantage that the right-hand side of (9) is very small for large y. Note that we could write that the velocity field is $U_0 + U_1 + U_3$, and that a term $U_2 \times (\omega_0 + \omega_1 + \omega_3)$ is added in the fringe. This would also yield (9), but may seem more arbitrary than the interpretation of U_2 as a field with negative divergence designed to remove low-momentum turbulent fluid. The last term in (9) was added after it was found that the energy of the fluctuations was boosted in the fringe, presumably because of the compression by v_2, resulting in an overshoot of the shear-stress profile at the inflow. With that term included the stress profiles are in better agreement with experiment at $x = 0.4$, although still not monotonically decreasing (figure 11a, below). In retrospect, a larger value of S', and some adjustment near the wall, would have been preferable. Prospective users should discard this term, unless there is a very clear need for it.

3.3. *Control of the pressure distribution*

The quantity $U_{3\mathrm{w}}$ is computed by considering the slip velocity of the total velocity field $U_0 + U_1 + U_3$. There is no need to consider U_2 in the useful region. Recall our definition of the slip velocity as the extrapolation to $y = 0$ of the velocity in the irrotational region. The contribution of U_0 is $U_{0\mathrm{w}}$, because the $\exp(-y/y_3)$ term of ($7a$) is zero in the irrotational region, and because ky_2 is small so that $\cosh(ky_2)$ is very close to 1.

As for U_1, it can be shown that in the irrotational region

$$\hat{u}_1(k, y) = -I(k) \exp(-ky),\tag{10}$$

where

$$I(k) \equiv \int_0^\infty \hat{\omega}_{z1}(k, y') \sinh(ky') \, \mathrm{d}y'.\tag{11}$$

This comes from the Poisson equation $(\partial_{yy} - k^2)\hat{v}_1 = \mathrm{i}k\hat{\omega}_{z1}$, the boundary conditions on U_1, and the continuity condition. Now the extrapolation of (10) down to $y = 0$ is $-I(k)$. This means that the field U_1, even though it tends to zero both at the wall and far from it, contributes a slip velocity. The role of U_3 is to offset it, and therefore we write

$$\hat{U}_{3w}(k) = I(k).\tag{12}$$

When $k = 0$, (10) and (11) are not valid. However, in that case $\hat{u}_1$ is zero in the irrotational region, so that its extrapolation to the wall is zero. Thus we can still apply (12) since $I(0) = 0$.

The mission of U_3 is to offset fluctuations of the slip velocity on a large spatial scale, but not to suppress short-scale turbulent fluctuations. Accordingly, after I is computed from ω_1 it is filtered before it is assigned to $\hat{U}_{3w}$. The spatial filter used is the Gaussian $\exp(-0.03[k/k_0]^2)$, where $k_0 \equiv 2\pi/\Lambda_x$ is the lowest wavenumber. The coefficient 0.03 is not critical. Once the flow has reached a statistically steady state, the filtered version of I is essentially time-independent. This is why $\partial U_3/\partial t$ was omitted in (9). Note also that U_3 is smooth in x, and independent of z.

3.4. *Numerical resolution, initial conditions, and transient behaviour*

The periodic domain in x is [0.3, 1.1] (i.e. $x_0 = 0.3$ and $\Lambda_x = 0.8$) and $x_1 = 0.04$, so that the useful region, or 'comparison region', is [0.4, 1] (figure 1). Only the wavenumbers 0 to 4 are retained in $\hat{U}_{0w}(k)$. The aim is for the simulation slip velocity to match the experimental one in the useful region, and smoothly return to the inflow value within the fringe. This is achieved through a least-squares fit to the experimental slip velocity, obtained from the Bernoulli equation, over the useful region. Points every 0.05 in the region [0.4, 1] are given equal weights in the least-squares equation. The point $x = 1.05$ is given a smaller but non-zero weight, even though it is outside the useful region, to help sustain the APG up to $x = 1$. The cosines have coefficients 1.0827, -0.0815, -0.0059, -0.0029, and -0.0010; the sines have 0.0637, 0.0017, 0.0057, and 0.0032. More waves would marginally improve the fit, but also generate larger velocities for large y because of the exponentials in (7). The I-terms are of magnitude 0.015 at most, fitting their description as small but not negligible corrections.

The y_0-scale in the exponential mapping is 0.012, y_2 is 0.0024, and the period in z is 0.09, or about three times the maximum boundary-layer thickness $\delta_{\max}$. This is comparable with values used earlier (Spalart 1988a). With zero pressure gradient the value $\Lambda_z/\delta \approx 3.75$ was adequate, and here the mean straining transports turbulence upward so that the ratio of width to height, for the large coherent structures, is smaller. The two-point correlations suggest that the width of the large eddies at $x = 1$ is about 0.02. To obtain the same resolution as in past studies (Spalart 1988a), measured in wall units based on the highest value of u_τ (near $x = 0.53$), the number of quadrature points in x, y, and z is $960 \times 82 \times 320$ (the numbers of spectral modes in each direction is $\frac{2}{3}$ the number of points). The fringe parameters (normalized by U_{ref} and metres) are $S = 10$ and $y_1 = 0.00025$.

The simulation was started on a coarser grid ($432 \times 64 \times 160$), with $U_1 = 0$ and

finite-amplitude random body forces, active for only one time step and only near the wall. The goal is to 'stir' the fluid and introduce short length and time scales immediately, but without contaminating the free stream. The simulation proceeded on successively finer grids for a time of about 6, undergoing manual adjustments of the fringe parameters such as S, at which point it was ready for transfer to the fine grid and sampling. In 6 time units free-stream particles travel around the period (A_x) about 8 times; the boundary-layer structures and other information propagate more slowly, so that they may have gone around about 3 times, which is enough for a globally steady state to be established. The sampling time was 0.81 (normalized by U_{ref} and metres), or about 25 times δ_{max}/U_{ref}. 100 velocity fields, evenly spaced, were used and saved for future studies. The simulation time step was about 0.00024. The fine-grid run consumed about 300 hours on a Cray Y-MP, single processor. The sampling domain in z was of course $A_z = 0.09$. A bell-shaped filter of width about 0.02, in the x-direction, was applied to the statistics before plotting. The data before filtering were smooth enough to bear out all the conclusions of the study, but the filtering made them more suitable for presentation.

3.5. *Initial assessment of the fringe method as an inflow–outflow system*

Simulations of boundary layers with inflow–outflow conditions have been performed by Fasel (1976; also Konzelmann & Fasel 1991), Streett & Macaraeg (1989; also Danabasoglu, Biringen & Streett 1991), and Rai & Moin (1991). At the inflow, Fasel & Streett use straightforward Dirichlet boundary conditions, which are favourable for small-amplitude waves. Rai & Moin use Dirichlet conditions for the incoming characteristics (they have subsonic inflow) to input synthetic free-stream turbulence, which then ages before encountering the plate. At the outflow, Fasel uses a condition on the second derivatives, which works well only for small-amplitude single waves. It is unlikely that that condition can be extended to tolerate a turbulent outflow. Streett & Macaraeg use a 'buffer domain' in which the Navier–Stokes equations are altered, which is similar to the fringe method. In the initial paper the size of the buffer domain was equal to that of the useful domain, but Danabasoglu *et al.* now report a buffer domain equal to only 30 or 40% of the useful domain. We have yet to see fully turbulent results from Fasel's or Streett & Macaraeg's methods.

Rai & Moin deal with the turbulent outflow by progressively coarsening the grid in the streamwise direction, and then applying a fairly crude condition on the pressure. Because it is applied far downstream and the x-dependence has been suppressed, this condition is successful in terms of avoiding reflections. This is a kind of a buffer domain; by our estimate it uses up only about 15% of their grid points. Unlike our Fourier method, the finite-difference methods provide flexibility of the grid spacing. The upwind bias in Rai & Moin's finite-difference scheme probably helps prevent the propagation of the errors incurred in the region of grid coarsening.

This review reveals a strong trend towards buffer or fringe approaches to the outflow problem. These approaches may be vaguer and less pleasing than combinations of derivatives, but the latter conditions, abruptly applied at the end of the domain, have simply not been very successful when applied to general disturbances and turbulence.

The waste of grid points in the fringe region is not a serious concern, because the fringe method allows the use of Fourier series in x, which is very advantageous in terms of accuracy, storage, and numerical convenience (decoupling of modes in the linear terms). Such differences can easily bring about several-fold reductions in the computational effort required, so that a waste of even a quarter of the points in x is

very acceptable. In addition we show later that the turbulence at the inflow is quite normal, and synthetic turbulent inflow conditions of comparable quality have yet to be obtained.

The computer time per grid point and time step for the methods of Fasel's group (U. Konzelmann and U. Rist, personal communication, 1991) and of Danabasoglu *et al.* (1991) ranges from about 3 to 12 μs on Cray supercomputers. The present simulation, even though it suffers from the $O(N_y^2)$ scaling (Spalart *et al.* 1991), needs 4.1 μs for each substep of the Runge–Kutta scheme, on a recent Cray Y-MP. The accuracy advantage of the spectral method amounts to an advantage of at least a factor of 2 in each direction. For instance, in stability work we use about 10 points per wavelength even with rapid amplification (without amplification, 3 points per wave are sufficient). Danabasoglu *et al.* (1991) and Konzelmann & Fasel (1991) use between 32 and 40 points per wavelength in their fourth-order-accurate methods. Konzelmann & Fasel use 105 points in the y-direction, again with fourth-order accuracy, whereas spectral methods need only 25 to 40 points for accurate stability results (Spalart *et al.* 1991; Danabasoglu *et al.* 1991). Some methods also demand surprisingly large numbers of time steps, such as 750 to several thousand per period (Konzelmann & Fasel 1991; Danabasoglu *et al.* 1991). This cannot be required for accuracy. These stability difficulties are related to the spatial discretization and the rather large number of points (compounded by the wall suction and the Chebyshev discretization in the case of Danabasoglu *et al.*), and also the use of the Adams–Bashforth scheme at too high a Reynolds number.

The important issue is whether the flow in the useful region is disturbed by the violation of the equations in the fringe. The essential arguments are that the vortical region (the boundary layer) is thin compared with the streamwise distances, and the presence of the wall. Let us expand. We have seen in §3.3 that the long-range variations of the free-stream flow (specifically, the slip velocity) are controlled. Therefore, provided that vorticity does not escape the wall region (which we verify) the evolution of the unknown field U_1 under (9) amounts only to displacing vorticity within a shallow region of thickness δ. If we reason in terms of velocity induced by vorticity we find that this vorticity and its image vorticity (because of the wall) form a dipole so that the velocity they induce at a distance Δx upstream or downstream, within a distance δ of the wall, decays like $(\delta/\Delta x)^2$ for the u-component, and $(\delta/\Delta x)^3$ for the v-component. This shows that a change in the vorticity field within the boundary layer, with the free-stream velocity held fixed, is not felt farther away than a few boundary-layer thicknesses. Thus, at the interface, vorticity flows into the useful region closer to the wall thanks to the fringe terms, but the exact mechanism that effected the thickness reduction (here, the $U_2 \times (\omega_0 + \omega_1 + \omega_3)$ term, but it could have been wall suction) is not important. In fact the removal of boundary-layer fluid by suction is used in many experiments, and the boundary layer is not considered to be durably suspect downstream of the slot, let alone upstream of it.

Another benefit of boundary-layer physics is that, although the direct effect of v_2 is to blindly reduce the size of the layer in the y-direction, turbulent structures are constantly destroyed and regenerated so that the lengthscales in x and z, and the timescales, adapt to the imposed y-scale. This effect is probably largely responsible for the fair quality of the turbulence at the inflow (see figures 9–14). Note also that v_2 (having a double zero at the wall) is very small in the wall region of the boundary layer; for instance at $y^+ = 25$, $v_2^+ \approx -0.09$ compared with $U^+ \approx 12$ and $v'^+ \approx 0.8$.

Let us examine two other possible candidates for a fringe treatment. We could attempt to simulate decaying grid turbulence, with periodicity in y and z, and it

would be an easy matter to enhance the turbulent energy in the fringe. However, the lengthscales also increase during the decay and the large-scale motion would need to be suppressed, so that it does not outgrow the periods in y and z. There would be little benefit from 'recycling' the turbulence. A mixing layer would be a somewhat better proposition since we could reduce the thickness with a v_2-field as in the boundary layer, but the larger timescales introduced by pairing could hardly be eliminated, resulting in a spurious feedback mechanism. There is not as rapid a turbulence regeneration as in the boundary layer, nor is there a wall to suppress long-distance interactions in x. We do not recommend the fringe method except for boundary layers and similar flows (channel, pipe).

In addition to the physical issues addressed so far there is a numerical issue. Large numerical errors in the fringe would easily contaminate the useful region, especially with a spectral method. Therefore we must ensure that the fluctuations in the fringe do not become either much more intense or much more difficult to resolve (because of steep gradients) than those in the useful region. Such a phenomenon would be fairly easy to detect, however.

A disadvantage, relative to the multiple-scale method (Spalart 1988a), is the loss of statistical sample and of spectra in x. This makes it more difficult to obtain smooth statistics. In addition, although the programming of (7)–(12) and the extraction of simple statistics up to Reynolds stresses is straightforward, the extraction of the Reynolds-stress budgets, for instance, is not. Another unpleasant feature is the large number of arbitrary functions and fringe parameters that had to be introduced. A few of these are being improved, simplified, or eliminated. This work being the first inflow/outflow simulation with the fringe method, we had to also report the more awkward aspects of the approach, such as the S' term. The major obstacle to the optimization of the method is the small number of simulations that are being conducted: only four to date.

In summary it is very plausible based on the arguments just presented and on practical evidence that for a boundary layer the fringe method indeed allows a solution of the Navier–Stokes equations in the useful region without significant spurious interactions across the fringe. In addition the 'recycling' of the turbulence across the fringe yields inflow turbulence of rather high quality. Compared with the multiple-scale method the new method has the major advantage that the equations are 'pure' in the useful region, and that steep pressure gradients can be treated. Compared with conventional inflow–outflow procedures, it is very likely that the fringe method requires a shorter entry length for the turbulence to be well-developed. In addition, the outflow condition has never caused any loss of numerical stability. Finally, note that all turbulent outflow approximations rely on equations that are at best plausible, and have little to do with the Navier–Stokes equations.

4. Results

4.1. *Global quantities*

The wall-pressure coefficient of the experiment (EXP) and of the simulation are compared in figure 2 over the full periodic domain of the DNS [0.3, 1.1] to illustrate the fringes. The declared 'comparison region' is [0.4, 1]. The agreement within it is very good since the difference is at most 0.01. Had the interaction term $I(k)$ been omitted, the C_p would have shown errors of up to 0.05 near $x = 1$. We reiterate that, unlike in a Reynolds-averaged boundary-layer calculation, the agreement shown in figure 2 is not trivial. The difficulty was to obtain a specified distribution of the *mean*
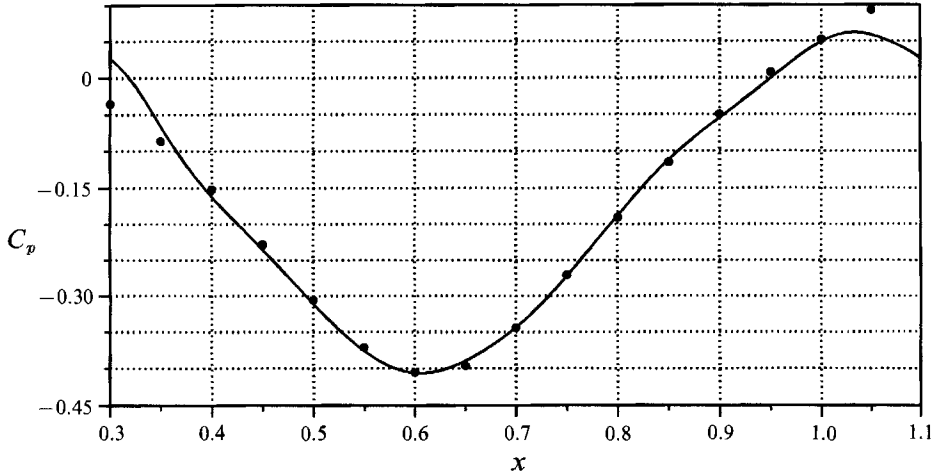
FIGURE 2. Mean wall-pressure coefficient, based on U_{ref}. ●, EXP; ——, DNS.

pressure without holding any *instantaneous* quantity. The results vindicate the route taken with the slip velocity, and the interaction through $I(k)$.

The pressure within the flow was extracted from the simulation. The largest differences relative to the wall pressure were found near $x = 0.6$. As expected from the concave curvature of the streamlines, the static pressure at the edge of the boundary layer was lower than the wall pressure, by about 0.01 in C_p. This is a concern in the experiment (§2.4). The effect on Pitot-tube measurements of velocity was computed from the simulation, i.e. we compared U and $[U^2 + 2(p - p_w)/\rho]^{\frac{1}{2}}$. Even at $x = 0.6$ the errors were negligible within the boundary layer, and reached only a few percent far outside the boundary layer ($y \approx 3\delta$).

The displacement and momentum thicknesses are considered next. To compute them with the classical definitions (integrals of the velocity) we need a value $y = \delta$ at which to truncate the integrals, and to give the edge velocity. This value is much more critical here than in boundary-layer calculations because, as mentioned before, $U(y)$ does not tend to a constant as $y \to \infty$. Outside the vortical region it shows a curvature, which may be of either sign, so that definitions such as the location at which U is 99.5% of free stream may fail completely. This is due to the pressure gradient, and is admittedly exacerbated near the right fringe because of the rapid turnaround of the C_p (see figure 10d below).

Two remedies were applied. The first was to prescribe a function $\delta(x)$, adjusted manually to be between 20 and 30% above the edge of the turbulent region, meaning the region with significant vorticity and Reynolds shear stress. The value of δ will be indicated on later plots, allowing the reader to judge the quality of the fit. The formula is

$$\delta = 0.015 + 0.023x^2. \tag{13}$$

The second remedy was to base the definitions of the thicknesses on the vorticity. Within the boundary-layer approximation ($\omega_z \approx -u_y$) and using integrations by parts the edge velocity U_∞ and the thicknesses can be written

$$U_\infty \equiv -\int_0^\infty \omega_z(y)\,\mathrm{d}y, \quad \delta^* \equiv -\frac{1}{U_\infty}\int_0^\infty y\omega_z(y)\,\mathrm{d}y,$$

$$\theta \equiv \frac{2}{U_\infty^2}\int_0^\infty y\left[\int_0^y \omega_z(y')\,\mathrm{d}y'\right]\omega_z(y)\,\mathrm{d}y - \delta^*. \tag{14}$$

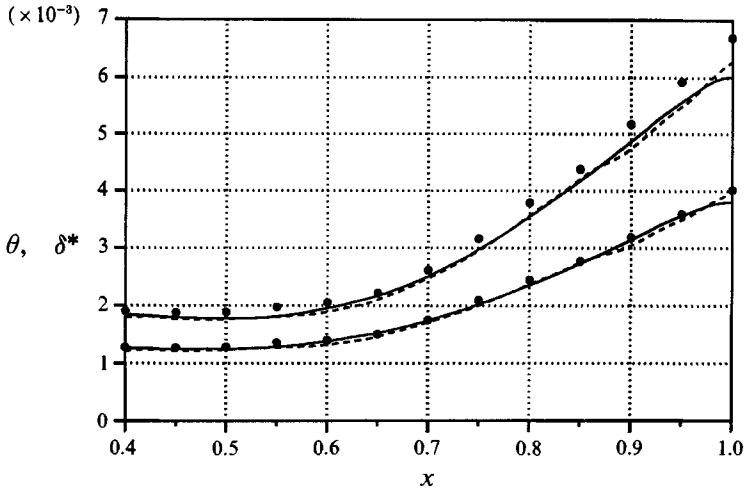FIGURE 3. Momentum and displacement thicknesses. Lower curves, θ; upper curves, δ^*. ●, EXP; —— , DNS, velocity integrals truncated at δ (13); – – –, DNS, vorticity integrals (14).
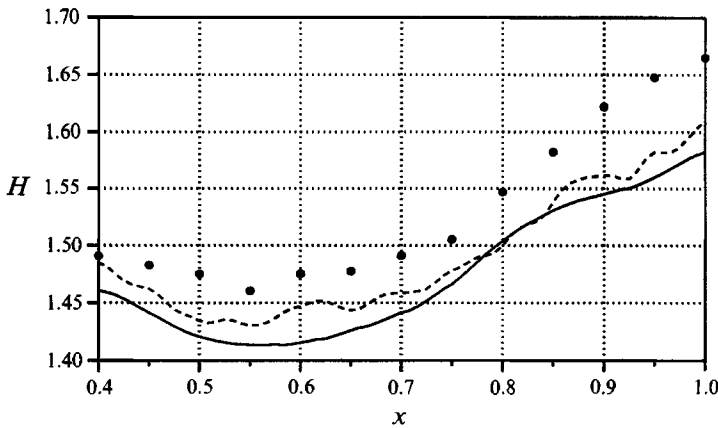

FIGURE 4. Shape factor. Symbols as in figure 3.

These definitions illustrate the interpretation of δ^* as the centroid of vorticity, and they are well-behaved in pressure-gradient flows, because unlike $\partial U/\partial y$ the vorticity decays fast enough as $y \to \infty$ for the integrals to converge. Unfortunately, we have been unable to extend these definitions to compressible flow. We were also unable to obtain the vorticity accurately enough from the experiment, even by computing v from the continuity equation and then differentiating it in x. On the other hand, the vorticity integrals converged well for the DNS. Figure 3 shows that thicknesses obtained from the classical definitions and from (14) agree well. The vorticity thicknesses are a little noisier, but they are better behaved near the right fringe.

The thicknesses are shown in figure 3 and the shape factor in figure 4, and the agreement with experiment is fair. The thicknesses were successfully matched at the inflow, $x = 0.4$, but the DNS values for δ^* and H soon drop below the EXP values. The DNS value for H at $x = 0.5$ is about 1.43. This is consistent with the value in a sink flow with $K = 1.25 \times 10^{-6}$, which is between 1.38 and 1.43. The EXP values are around 1.47. Subsequently the two data sets seem not to resolve the difference, with
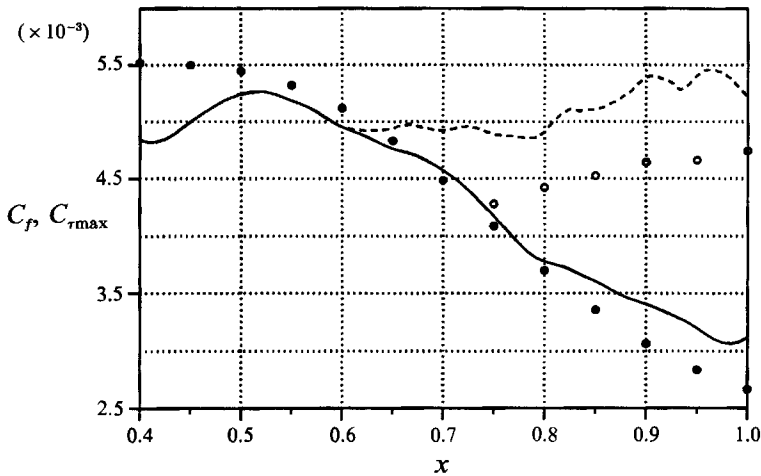
FIGURE 5. Shear-stress coefficients, based on U_∞. ———, DNS wall stress; — — —, DNS peak stress (versus y); ●, EXP wall stress; ○, EXP peak stress.

the shape-factor difference even compounding a little in the APG. The velocity profiles presented later (figure 9) show that the thicknesses tend to emphasize differences that are detectable, but rather subtle.

The skin-friction coefficient C_f based on U_∞ is shown in figure 5, and the quality of the agreement is about the same. Here the velocity U_∞ was computed from the wall pressure using Bernoulli's equation ($U_\infty = U_{\text{ref}}(1 - C_p)^{\frac{1}{2}}$); therefore, in view of figure 1, the comparison is not biased by sizeable differences in U_∞. In figure 9 below it is shown that, had the measured value of U at the edge of the boundary layer been used instead, the EXP result for C_f would be slightly lower, by up to 4 %. This would benefit the agreement between 0.55 and 0.7, and degrade it beyond 0.7. The DNS value is definitely too low at $x = 0.4$. The wall region lost energy, possibly due to the S' term which was aimed at the upper region. The skin friction recovers by $x = 0.55$. After this we observe disagreements of up to 3.5×10^{-4}, which is 12 % at $x = 1$. The disagreement is fully correlated with the pressure gradient and will be discussed further.

The peak value of the total shear stress across the boundary layer, τ_{max}, is also shown in figure 5. In an FPG the peak is reached at the wall, so that $C_{\tau\text{max}} = C_f$. In the experiment the skin friction and the shear stress in the field are obtained by different means, which explains why the two curves do not smoothly diverge when the APG is applied. This is discussed further below. Note that the ratio $C_{\tau\text{max}}/C_f$ reaches about 1.7; the value 1.5 is sometimes quoted as the minimum needed for the flow behaviour to be typical of an APG (Schofield 1981).

Figure 6 shows the momentum balance – within the boundary-layer approximation – for both datasets, $P_L \equiv (1 - C_p) \theta - \int \frac{1}{2} \delta^* \, dC_p$ and $P_R \equiv \int \frac{1}{2} C_f \, dx$ versus x (C_f based on U_{ref} here, and vorticity thicknesses for the DNS). The P_L curves were translated to yield the same average over $[0.4, 1]$ as the corresponding P_R curves (each curve involves an arbitrary additive constant, because the origin of the integrals is arbitrary). The experimental and simulation curves are shifted with respect to each other for clarity. The balance is satisfactory in both cases, although noisier in the DNS.

Note that lack of balance has different causes in the two approaches. In experiments, it usually comes from imperfect two-dimensionality of the mean flow,
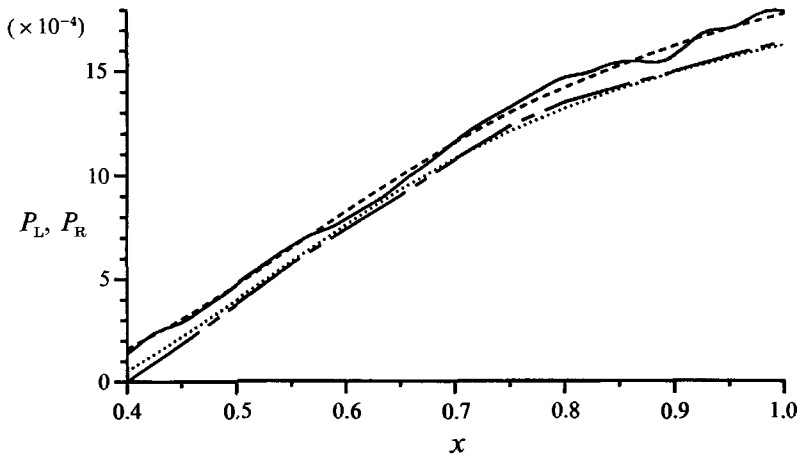
FIGURE 6. Momentum balance. ——, DNS P_L; – – –, DNS P_R; — —, EXP P_L; $\cdots$, EXP P_R.
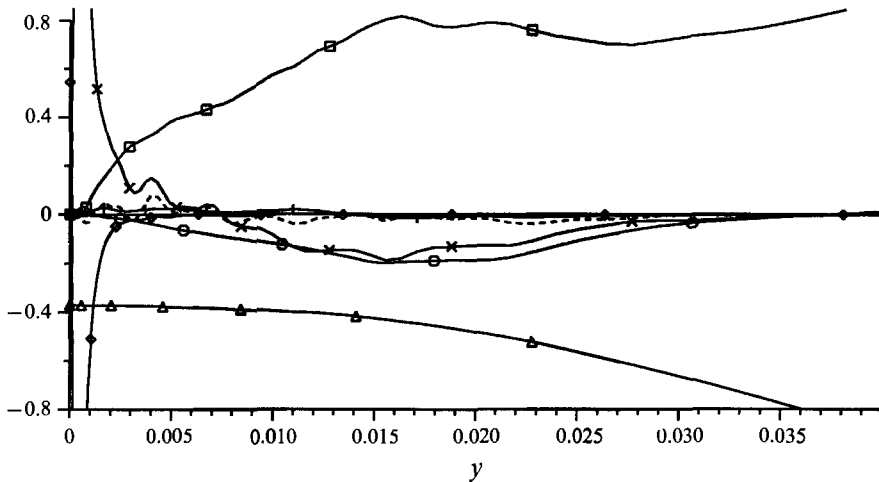

FIGURE 7. DNS momentum balance, at $x = 1$. $\square$, $-UU_x$; $\bigcirc$, $-VU_y$; $\triangle$, $-p_x$; $\diamond$, $\nu(U_{xx}+U_{yy})$; $+$, $-\partial_x \overline{u'^2}$; $\times$, $-\partial_y \overline{u'v'}$; – – –, sum.

or inaccurate measurements, particularly of C_f. In the simulation, lack of balance can come from a failure to reach a steady state, and/or insufficient length of the time sample. The effects of normal Reynolds stresses have been shown to be smaller than the differences we are observing here (Samuel & Joubert 1974). The uncertainty in the thicknesses is far from negligible. The DNS balance would be noticeably worse in the [0.8, 1] region if the velocity thicknesses were used.

The momentum-balance question is investigated in figure 7 with a representative detailed momentum balance from the DNS. The normal-stress term $-\partial_x \overline{u'^2}$ is indeed small. The sum of all terms is consistently much smaller than the dominant terms, showing that the flow has in fact reached steady state. We do not observe any trend such as an extended imbalance that would indicate that the flow has a sizeable $\partial\delta^*/\partial t$ (this quantity is the integral of the sum of the terms in figure 7). We do observe that the pressure gradient term $-p_x$ is not constant across the layer. Thus, at this value of x the boundary-layer approximations are not satisfied accurately enough for the
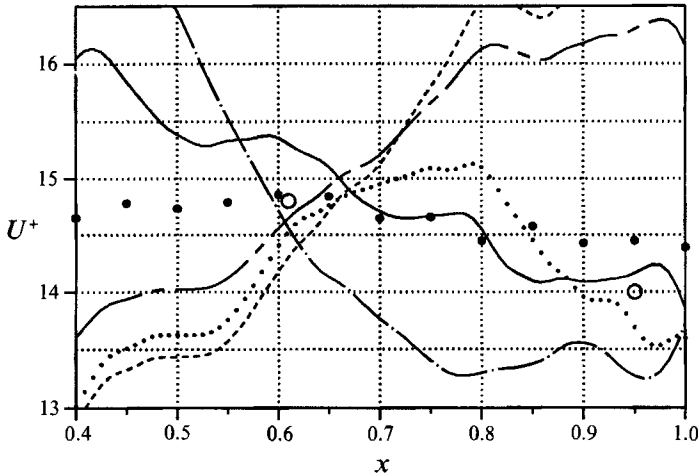
FIGURE 8. Value of U^+ at $y^+ = 50$. ●, EXP; ——, DNS; ○, Nagano *et al.*, at roughly the same pressure gradient; — — —, mixing-length formula, Van–Driest damping; ·—·, mixing-length formula, modified Van-Driest damping; – – –, Mellor–Herring formula; ···, Johnson–King formula.

$P_{\rm L}$–$P_{\rm R}$ plot (which uses the pressure gradient at the wall) to truly reflect the momentum balance. This waviness in the pressure in the upper part of the layer is found only close to the right fringe.

4.2. Skin-friction measurement and logarithmic layer

The 12% disagreement in skin friction at $x = 1$ is of concern. In the zero-pressure-gradient flow, the largest disagreement between DNS results and the average of experiments collected by Coles (1962) was about 5% (Spalart 1988a). In a simulation, there is no difficulty in computing the C_f. It is as reliable as the simulation as a whole. Grid-refinement tests conducted in the past (Spalart 1988a) indicate that the resolution used here, in wall units, is adequate in the FPG region and more than adequate in the APG region since the friction velocity has dropped by over 30% (in addition, from past experience we would expect numerical under-resolution to produce excessive skin friction in the FPG region, where u_τ is largest). This assumes that the wall region is no more difficult to resolve here than with zero pressure gradient. Admittedly the dissipation is higher in wall units, making the Kolmogorov scale smaller, but since only the power $\frac{1}{4}$ of the dissipation enters the lengthscale this effect is weaker than the drop of u_τ.

In the experiment a Preston tube is used to measure the skin friction; this is an indirect method that relies on the law of the wall. We explore this issue in figure 8 by plotting the value of U^+ at $y^+ = 50$, using the declared values of C_f in each dataset. The EXP points vary up, then down, but they are all between 14.4 and 14.8. In contrast the DNS results decrease steadily from about 15.4 at $x = 0.55$ (where we believe the inner layer is well developed) to about 14 at $x = 1$. Now, the recent literature contains values from 0.40 to 0.41 for κ, and from 5 to 5.2 for C, leading to a much narrower range for U^+ at $y^+ = 50$: 14.54 to 14.98. Nagano *et al.*'s results, at roughly the same value of p^+ and β and a comparable Reynolds number, agree fairly well with the DNS results. The shift they observed is about 30% smaller. Note that they deduced the skin friction from single-wire measurements in the region $1.1 < y^+ < 5$, with a very substantial correction for near-wall effects. The correction was

calibrated with zero pressure gradient (obtaining the skin friction by Clauser's method), within the same experimental set-up.

The shift up slightly beyond 15 in the FPG is consistent with experimental and DNS results in sink flows (Jones & Launder 1972; Spalart 1986) and channel flows (Antonia *et al.* 1992). However, in those flows, the Reynolds number and the pressure gradient are not independent. The present DNS results, which independently support Nagano *et al.*'s results, strongly suggest that the shift is a pressure-gradient effect. If so, it illustrates again the irrelevance of near-wall Taylor expansions anywhere outside the viscous sublayer: the second-order Taylor expansion $U^+ = y^+ + \frac{1}{2}p^+y^{+2} + O(y^3)$ (recall that $p^+ \equiv \nu p_x/u_\tau^3$) shows that close enough to the wall the U^+ profile is higher in an APG (see also figure 10 below). The cross-over point is near $y^+ = 8$.

Early DNS results with pressure gradients (Spalart & Leonard 1986) also showed a shift of the U^+ profile. It was of the same magnitude as the present one, and also became noticeable near $y^+ = 10$, except for a very strong APG ($p^+ \geqslant 0.15$). These results led to the same conclusions as here, but we placed less confidence on them, because of the multiple-scale approximation. At the time the method used the law of the wall as an assumption, and then mildly disproved it, leaving a confused picture. This weakness has been eliminated.

The shift down in the APG region is in agreement with some results of Hirt & Thomann (1986). However, they were considering sudden application and removal of pressure gradients, and they report errors of either sign in an APG. The current flow is gradual (p^+ ranges from -0.008 to $+0.02$) and thus only a subset of the range of situations they were exploring. Frei & Thomann reported a shift down by up to 1.5 units of U^+, but also a shift up after the APG is also completely removed. Both studies used an elaborate balance for direct skin-friction measurement, but showed considerable caution in trusting its predictions. Hirt & Thomann disproved an empirical formula due to Frei & Thomann, but only by using steep pressure gradients. However, the formula predicts a shift up for the velocity profile in an APG, and therefore disagrees with the DNS and Nagano *et al.*'s results.

Let us add the present DNS results to the body of evidence for a moderate failure of the law of the wall in pressure gradients. This body is still small and far from sorted out. We cannot draw conclusions valid in the large-Reynolds-number limit. For instance, the apparent log layer is much too short to give hope of separating the effect of κ and C; this is why we sought a substantial quantity, namely $U^+(50)$, for figure 8. In addition, at $y^+ = 50$ the total shear stress already departs from its first-order Taylor expansion $\tau^+ = 1 + p^+y^+$ very strongly (in figure 11*d*, $y^+ = 50$ corresponds to $y = 0.0032$), indicating that a correction (such as the 'modified damping', below) based solely on p^+ should certainly not be generalized from the present dataset. Much higher Reynolds numbers are needed, as are larger values of p^+.

Nevertheless, a survey of the more widespread turbulence models gives food for thought. Figure 8 shows the value at $y^+ = 50$ of the velocity profiles that each model would associate with the total shear stress τ extracted from the DNS. For instance, for the mixing-length model with Van-Driest damping we calculated

$$U^+_{\text{model}}(50) = \int_0^{50} \frac{2\tau^+}{1 + (1 + 4\tau^+ l^{+2})^{\frac{1}{2}}} dy^+ \quad \text{where} \quad l^+ = \kappa y^+[1 - \exp(-y^+/26)]. \quad (15)$$

The results are shown in figure 8 for the mixing-length model with Van-Driest damping, and with a modified damping; the Mellor–Herring model (Coles & Hirst

1968); and the Johnson–King model, for which we used the 1985 version except that A^+ was taken as 17 as in later versions. The 'modified damping' loosely follows the type of formulae reviewed by Cebeci & Smith (1974), but includes only a first-order effect of p^+. It consists of substituting $26/(1+\alpha p^+)$ for 26 in (15), where α is a constant discussed below.

The curves all agree well near $x = 0.63$, where the pressure has its minimum, although the outer region is not indicative of an established zero-pressure-gradient flow (see figure 11b). As already noted by McDonald (1968), except with modified damping, the older models predict a shift over the log law in APG, in sharp contrast with the DNS and Nagano *et al.*'s results. In fact the shift from $x = 0.5$ to $x = 1$ is more than the opposite of that shown by the DNS. It is strongest for the Mellor–Herring model. The Johnson–King model reverses its trend as the pressure gradient switches sign, making it quite accurate in the APG. It benefits from the use of the outer-layer velocity scale $\tau_{max}^{\frac{1}{2}}$ in the inner-layer model, but forfeits the hope of an understanding in terms of near-wall quantities alone. The Johnson–Coakley model (1990) was devised specifically to obtain law-of-the-wall behaviour instead of mixing-length behaviour in APG, citing Galbraith & Head (1975). It gives a smaller eddy viscosity than Johnson–King, which puts its results a little farther from the DNS results. The α constant in the modified damping can be tuned to produce about the same shift as in the DNS results. The best value is about 45; Nagano *et al.* give 30.18, again about one-third smaller. Since p^+ takes values near 0.02, this correction is already very substantial and nonlinear in p^+, that is, $1/(1+\alpha p^+)$ and $(1-\alpha p^+)$ are quite different. We made no attempt to optimize the nonlinear trend, except for noting that the $(1-\alpha p^+)$ form breaks down completely for stronger gradients. In summary, we seem to confirm a qualitative deficiency of the widespread (unmodified) algebraic inner-layer turbulence models. However, it would be premature to make constructive suggestions, because of the lack of enough cases. Also, the importance in practice of this deficiency should not be inflated, because in strong adverse gradients the outer-layer model dominates.

The shift of the U^+ profile is of great interest for indirect methods of skin-friction measurement such as the Preston tube and the Clauser chart. Consider a hypothetical method that strictly consists of assuming that U^+ takes its standard value and slope at $y^+ = 50$, whereas in fact it is shifted by ΔU^+, the symbol Δ denoting a small error. Assume the dimensional velocity near $y^+ = 50$ is measured exactly. The result is

$$\frac{\Delta u_\tau}{u_\tau} = \frac{\Delta U^+}{U^+ + 1/\kappa}. \tag{16}$$

At $x = 1$ the DNS gives $\Delta U^+ \approx -1$, so the relative error in measuring the friction velocity is $\Delta u_\tau / u_\tau \approx -0.06$. Thus, the indirect method would underpredict the skin friction by 12%. While the Preston-tube system is not as simple as our hypothetical indirect method, it appears that this effect can account for about half of the 12% skin-friction disagreement between experiment and simulation (at $x = 1, \Delta U^+$ between EXP and DNS is about -0.5). The other half arises from genuine differences in the measurements, for instance near $y = 0.002$ in figure 9(d).

4.3. Local results

We show results at four stations: $x = 0.4$ gives inflow values for possible other investigators, and 0.6, 0.8, and 1 allow meaningful comparisons. The velocity profiles in figure 9 illustrate the shape-factor disagreement. The EXP values of U near the
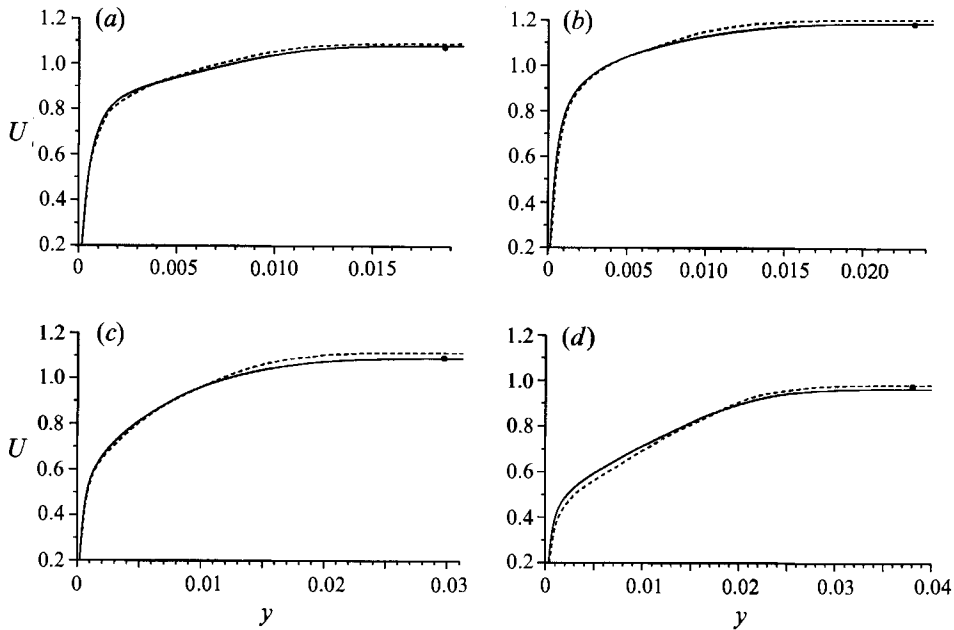
FIGURE 9. Velocity profiles, normalized by U_{ref}. ———, DNS; –––, EXP. (a) $x = 0.4$; (b) $x = 0.6$; (c) $x = 0.8$; (d) $x = 1$. ●, $y = \delta$ (13), $U = U_\infty$, from the Bernoulli equation.
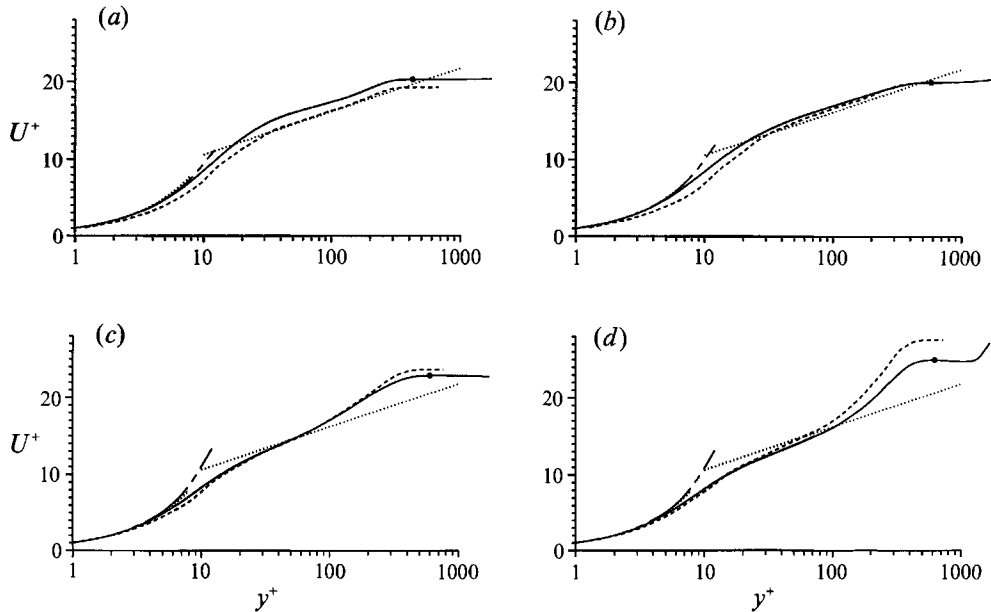

FIGURE 10. Velocity profiles, in wall units. ———, DNS; ————, EXP; ···, log law ($\kappa = 0.41$, $C = 5.2$) and $U^+ = y^+$ Taylor expansion; ————, $U^+ = y^+ + \frac{1}{2}p^+y^{+2}$ Taylor expansion. (a) $x = 0.4$; (b) $x = 0.6$; (c) $x = 0.8$; (d) $x = 1$. ●, locates δ (13).

edge of the layer are slightly higher, and farther from matching the value deduced from the Bernoulli equation. Figure 10 expands on figure 8 for the U^+ shift and displays the increased wake component in the APG. It also illustrates the rapid variations of U starting around $y = 0.07$ ($y^+ \approx 1300$, for $x = 1$), preceded by the drift discussed above in the context of the definition of the boundary-layer thicknesses.
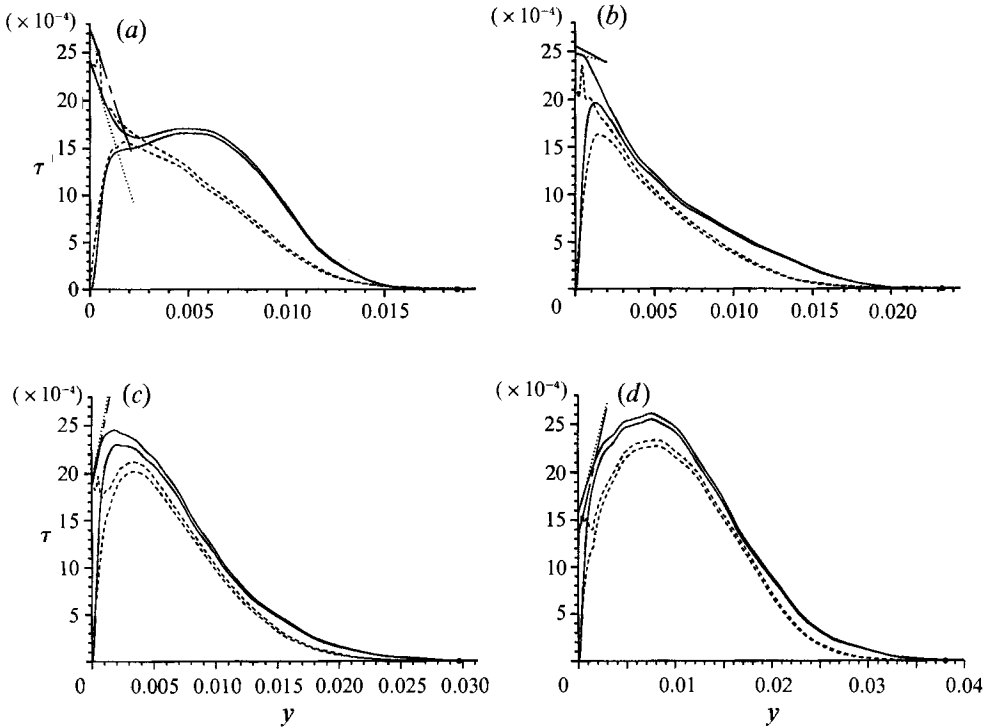
FIGURE 11. Reynolds and total shear-stress profiles. ——, DNS; ———, EXP; $\cdots$, $\tau = \tau_w + y\,\mathrm{d}p_w/\mathrm{d}x$ Taylor expansion for DNS; – – –, Taylor expansion for EXP. (a) $x = 0.4$; (b) $x = 0.6$; (c) $x = 0.8$; (d) $x = 1$.

Next we show the shear stress, in figure 11. The anomalous stress for the DNS at $x = 0.4$ was mentioned earlier (§3.2). The subsequent recovery is assisted by the FPG and is a credit to the design of the flow (Watmuff & Westphal 1989). Farther down, the DNS result is consistently higher than the EXP result. The peak values were shown in figure 5. The linear Taylor expansion of the total stress near the wall follows the DNS curve, consistent with the momentum balance in figure 7. Conversely, it brings out the near-wall difficulties of the experiment. There, we took the Preston-tube value of the skin friction. The Taylor expansion and the measured values do not connect well. This suggests that the viscous shear stress is unreliable near the wall, which was not unexpected, but also that the Reynolds-stress measurements in the upper layer are underestimates. This could be due to the out-of-plane velocity component, as discussed in §2.5.2. However, we can loosely infer from the behaviour of the mean flow (lower H) that the DNS had a slightly higher shear stress than the EXP. Thus the true experimental shear stress may be between the curves of figure 11.

The root-mean-square profiles in figure 12 give about the same impression. The agreement is best for u', which is usually measured more accurately because it relies on a normal hot wire instead of an X-wire. The spatial averaging by the hot wires (length up to 13 wall units) may also play a role. The DNS v' and w' are definitely larger than the EXP ones by $x = 1$. Both datasets satisfy the Corrsin–Kistler relationships (Stewart 1956), $\overline{u'v'} \approx 0$, $\overline{v'^2} \approx \overline{u'^2} + \overline{w'^2}$, fairly well outside the boundary layer. These relationships would be exact in the absence of streamwise inhomo-geneity (and assuming zero vorticity), and serve as an approximate check.

The structure parameter in figure 13, $a_1 \equiv -\overline{u'v'}/(\overline{u'^2} + \overline{v'^2} + \overline{w'^2})$ (Bradshaw,
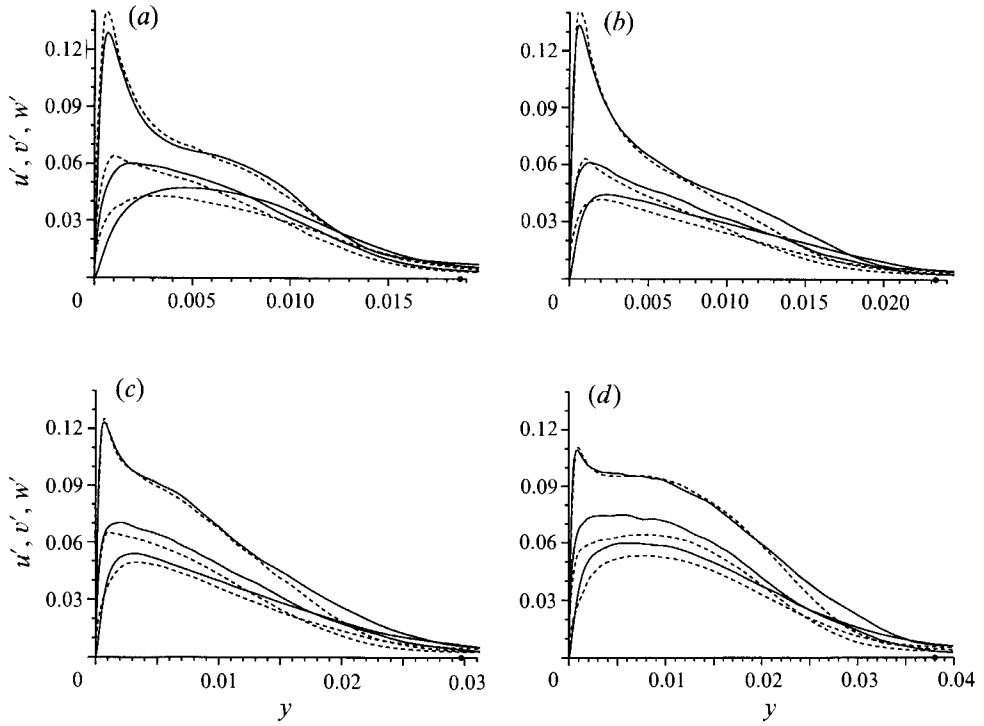
FIGURE 12. Root-mean-square profiles. ——, DNS; ----, EXP. Lower curves, v'; middle curves, w'; upper curves, u'. (a) $x = 0.4$; (b) $x = 0.6$; (c) $x = 0.8$; (d) $x = 1$.
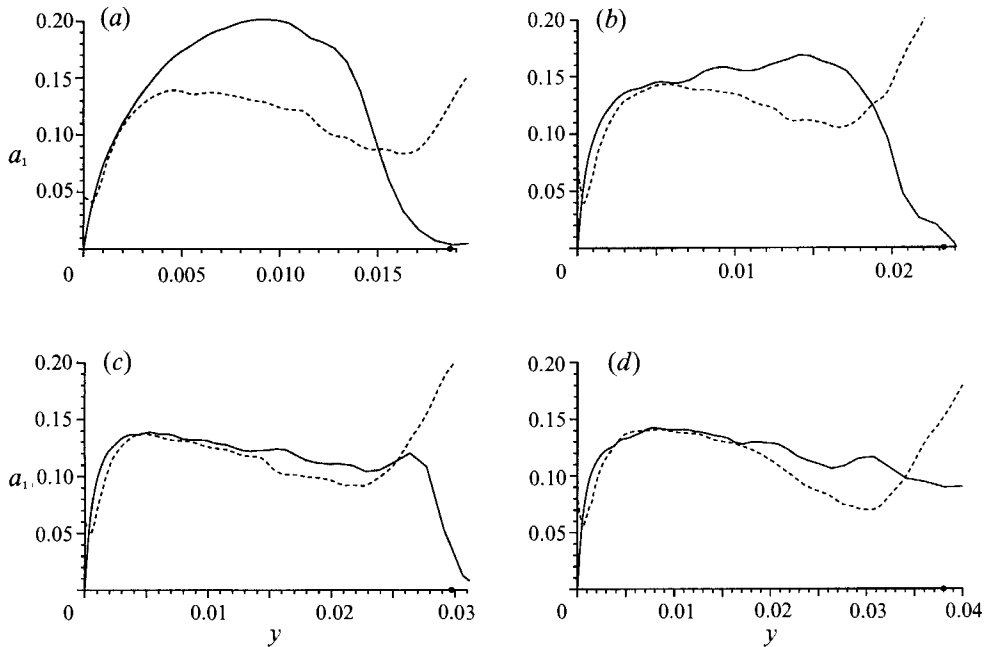

FIGURE 13. Structure parameter. ——, DNS; ----, EXP. (a) $x = 0.4$; (b) $x = 0.6$; (c) $x = 0.8$; (d) $x = 1$.
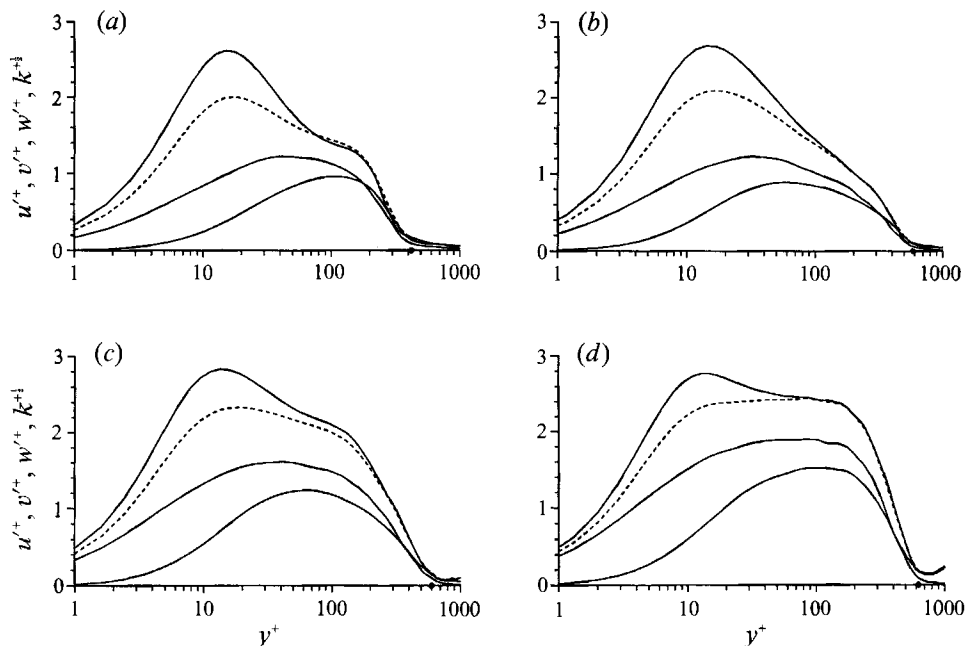
FIGURE 14. Root-mean-square profiles, in wall units, from DNS. ——, u'^+ (upper curves), w'^+ (middle curves), and v'^+ (lower curves); ———, $k^{+\frac{1}{2}}$. (a) $x = 0.4$; (b) $x = 0.6$; (c) $x = 0.8$; (d) $x = 1$.

Ferriss & Atwell 1967), shows extensive history effects in the DNS up to $x = 0.6$. Starting at $x \approx 0.7$ the two results agree well and show a consistent dip in the upper region. By $x = 1$ the value in the upper region is roughly 0.11 compared with the 'standard' 0.16. The largest values observed, near $y/\delta = 0.3$, are actually below 0.15. The EXP/DNS agreement is also a little misleading in that the numerators and denominators both disagree by up to 15%, in the same direction. The turn up of the EXP results near the edge of the layer is a little disappointing, in that the Corrsin–Kistler relationships require a_1 to drop to 0 outside the vortical region. Nonetheless, we consider the lowered values in the APG as established. The correlation coefficient R_{uv} has essentially the same behaviour. This conflicts with the results of Arnal, Cousteix & Michel (1976), for instance, even though they covered a wider range of APG (H up to 1.75).

4.4. Inner-layer scaling laws

Given complete near-wall fields from the DNS we can scrutinize the universality of that region, in addition to the test of U^+ shown above. Figure 14 details the behaviour of the root-mean-square intensities near the wall. From $x = 0.55$ to 1 the peak value of the streamwise intensity, u'^+_{max}, rises by about 0.2 both in EXP and DNS. In contrast the other components rapidly rise, in wall units, in the APG. The w' component is particularly sensitive, as found by Nagano *et al.* (1991) for a pressure gradient and by Spalart (1988a) for the Reynolds number. As a result the peak value of the turbulent energy, k^+_{max}, rises from about 4.2 to 6.2; see figure 15. In the past, it has been suggested that k^+_{max} takes the universal value of 4. The peak is reached near the wall, with y^+ less than 15, for $x < 0.95$; for larger x an upper peak develops (figure 14d). Even more striking is the behaviour of the wall dissipation ϵ^+_w, which more than doubles as shown in figure 16. Nagano *et al.* showed a similar effect on the
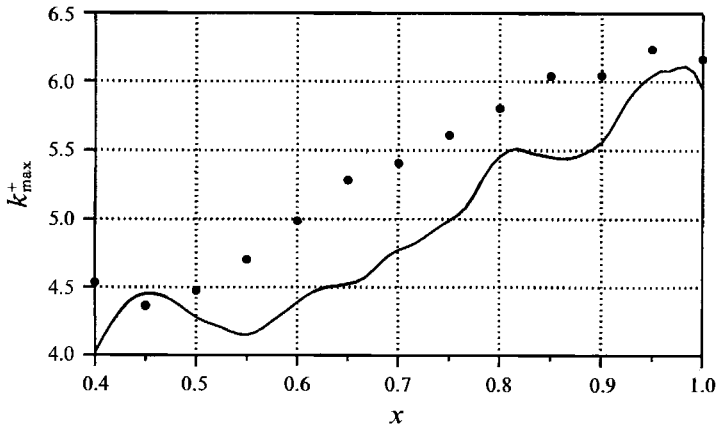
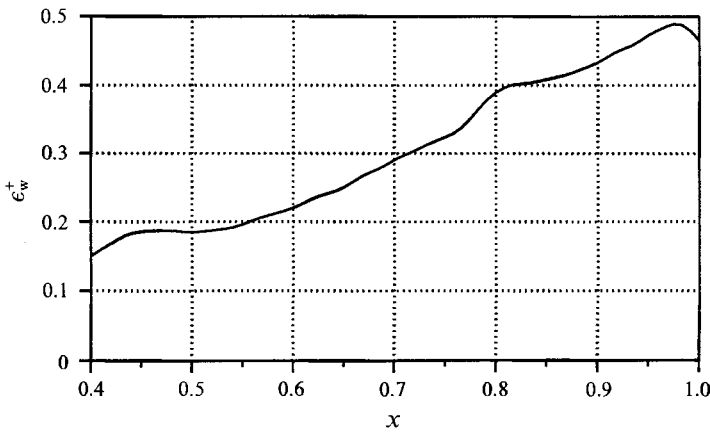FIGURE 15. Peak turbulent energy in wall units, k^+_{max}. ●, EXP; ——, DNS.

FIGURE 16. Wall dissipation in wall units, ϵ^+_w. ——, DNS.

near-wall streamwise fluctuations. At $y^+ = 1$ they obtain $u'^+ \approx 0.323 + 5.3 p^+$. At $x = 0.6$, 0.8, and 1 the values of p^+ are about 0, 0.013, and 0.015 respectively, so the formula gives 0.323, 0.39, and 0.40. The DNS yields 0.42, 0.50, and 0.51. Our values are higher, but the slope with respect to p^+ is about 6.1, which is not out of line with their 5.3.

Previous DNS results (Spalart 1988a) had shown lack of near-wall universality, due to the Reynolds number, but nothing of this magnitude. It does not come as a surprise that the pressure gradient would have a stronger effect than the Reynolds number, especially if the Reynolds number merely quadruples. Nevertheless, such a strong lack of universality is a major obstacle to theories and turbulence models.

5. Conclusions and future work

The outright comparison of experimental and direct-simulation results, conducted at the same Reynolds number and for a non-trivial turbulent boundary layer, is possible. The joint study provides an overall confidence in the results, an immediate estimate of the remaining uncertainty, and a picture so complete the readers can form their opinion about where the 'true' results lie.

The results are ready for use in the scrutiny of turbulence models, with a qualification. The Reynolds numbers ($R_\theta < 1600$) are well within the range that is

documented in zero pressure gradient as producing 'low-Reynolds-number effects' (Coles 1962). Consequently the straightforward testing and calibration of a model may not be the most judicious exercise. It may be that qualitative information is all that can be generalized with confidence to 'normal' Reynolds numbers.

Several qualitative facts do stand out. The first is that, according to the simulation, the U^+ profile in the buffer and lower log layer shifts up in a favourable pressure gradient, and down in adverse gradient. The experiment shows a much weaker trend in the same direction. The uncertainty in the measurement of the wall distance, which we estimate is close to 1 wall unit in this and in comparable experiments, remains a major obstacle to direct skin-friction measurements.

Sketchy theoretical arguments to the effect that the local total shear stress (instead of the wall shear stress) should enter the law of the wall, roughly equivalent to the mixing-length theory, make the profile shift in the direction opposite to what the DNS shows. In fact, the absence of a shift would have been even more remarkable than the observed shift is, because it would have suggested a simple situation 'waiting for an explanation' (see Galbraith & Head 1975). The shift is in fair agreement with the experimental results of Nagano *et al.* (1991). Their Reynolds number was not higher than ours. For once, the experimental incentive is also to lower the Reynolds number so as to thicken the viscous sublayer. Unfortunately, this means we have no way of distinguishing a buffer-layer effect from one that persists in the log layer. Nagano *et al.* concluded in favour of a buffer-layer effect, accounted for by the p^+ term in the modified Van-Driest damping, while the Kármán constant was unchanged. In our opinion, the log layers are too short and noisy for that question to be answered, if indeed there is a simple answer.

The somewhat unexpected behaviour of the U^+ profile is accompanied by other deviations from universal near-wall behaviour. The behaviour of the wall dissipation, for instance, is spectacular. Again its trend is in agreement with Nagano *et al.*'s results. Here the DNS evidence, as it did for the Reynolds-number effects (Spalart 1988a), opposes most theories as well as the application of wall functions in turbulence models, particularly for higher moments. It is in agreement with the inactive-motion ideas (Bradshaw 1967b), but these remain primarily qualitative. An uncontested quantitative model of turbulence in pressure gradients is far out of reach.

Another trend that may be a disappointment is the dip in the a_1 structure parameter in the upper part of the boundary layer in adverse pressure gradient. This does not instantly invalidate the turbulence model that relies on the universality of this ratio away from the wall (Bradshaw *et al.* 1967), because good models are rarely free of compensating errors. One should refrain from too literal an interpretation of the variables in models. Nevertheless, a dip across the whole width of the layer has often been attributed to three-dimensional effects. Here we observe a dip in a two-dimensional flow, but it is only in the upper part of the layer.

The original goal of improving on the results of Spalart & Leonard (1986) in adverse gradients has been achieved. The deviation of the velocity profile, compared with the experiment, is much smaller although still in the same direction. The DNS profile is slightly fuller. The cause of the earlier problems may remain a matter of conjecture, but the conjecture is of less importance now that the fringe method has superseded the multiple-scale method.

Future work will include a complete publication of the experimental results in the downstream region, where β is close to constant. The extension of the simulation to higher Reynolds numbers is not practical on current computers. We may conduct

further analysis of the flow fields and attempt to extract the Reynolds-stress budgets. It is not clear whether a sample long enough for that purpose can be generated.

REFERENCES

ANTONIA, R. A., TEITEL, M., KIM, J. & BROWNE, L. W. B. 1992 Low-Reynolds-number effects in a fully developed turbulent channel flow. *J. Fluid Mech.* **236**, 579–605.

ARNAL, D., COUSTEIX, J. & MICHEL, R. 1976 Couche limite se développant avec gradient de pression positif dans un écoulement turbulent. *La Rech. Aérosp.* **1976-1**, 13–26.

BRADSHAW, P. 1965 The effect of wind tunnel screens on nominally two-dimensional boundary layers. *J. Fluid Mech.* **22**, 679–688.

BRADSHAW, P. 1967 a The turbulence structure of equilibrium boundary layers. *J. Fluid Mech.* **29**, 625–645.

BRADSHAW, P. 1967 b 'Inactive' motion and pressure fluctuations in turbulent boundary layers. *J. Fluid Mech.* **30**, 241–258.

BRADSHAW, P., FERRISS, D. H. & ATWELL, N. P. 1967 Calculation of boundary-layer development using the turbulent energy equation. *J. Fluid Mech.* **28**, 593–616.

CEBECI, T. & SMITH, A. M. O. 1974 *Analysis of Turbulent Boundary Layers.* Academic.

CLAUSER, F. 1954 Turbulent boundary layers in adverse pressure gradients. *J. Aero Sci.* **21**, 91–108.

COLEMAN, G. N. & SPALART, P. R. 1993 Direct numerical simulation of a small separation bubble. In *Proc. Intl Conf. on Near-Wall Turbulent Flows, Arizona State U., March 15–17, 1993.*

COLES, D. E. 1956 The law of the wake in the turbulent boundary layer. *J. Fluid Mech.* **1**, 191–226.

COLES, D. E. 1957 Remarks on the equilibrium turbulent boundary layers. *J. Aero. Sci.* **24**, 495–506.

COLES, D. E. 1962 The turbulent boundary layer in a compressible fluid. Appendix A: A manual of experimental practice for low-speed flow. *Rand. Rep.*, pp. 35–74.

COLES, D. E. & HIRST, E. A. 1968 *Proc. AFOSR-IFP-Stanford Conf. on Computation of Turbulent Boundary Layers, Stanford, Aug. 18–25, 1968,* Vol. 2.

DANABASOGLU, G., BIRINGEN, S. & STREETT, C. L. 1991 Spatial simulation of instability control by periodic suction blowing. *Phys. Fluids* A **3**, 2138–2147.

DENGEL, P. & FERNHOLZ, H. H. 1990 An experimental investigation of an incompressible turbulent boundary layer in the vicinity of separation. *J. Fluid Mech.* **212**, 615–636.

FASEL, H. F. 1976 Investigation of the stability of boundary layers by a finite-difference model of the Navier–Stokes equations. *J. Fluid Mech.* **78**, 355–383.

FREI, D. & THOMANN, H. 1980 Direct measurements of skin friction in a turbulent boundary layer with a strong adverse pressure gradient. *J. Fluid Mech.* **101**, 79–95.

GALBRAITH, R. A. McD. & HEAD, M. R. 1975 Eddy viscosity and mixing length from measured boundary-layer developments. *Aero. Q.* **26**, 133–154.

HEAD, M. 1976 Equilibrium and near-equilibrium turbulent boundary layers. *J. Fluid Mech.* **73**, 1–8.

HERRING, H. J. & NORBURY, J. F. 1967 Some experiments on equilibrium boundary layers in favorable pressure gradients. *J. Fluid Mech.* **27**, 541–549.

HIRT, F. & THOMANN, H. 1986 Measurement of wall shear stress in turbulent boundary layers subject to strong pressure gradients. *J. Fluid Mech.* **171**, 547–562.

INMAN, P. N. & BRADSHAW, P. 1981 Mixing length in low Reynolds number turbulent boundary layers. *AIAA J.* **19**, 653–655.

JOHNSON, D. A. & COAKLEY, T. J. 1990 Improvements to a nonequilibrium algebraic turbulence model. *AIAA J.* **28**, 2000–2003.

JOHNSON, D. A. & KING, L. S. 1985 A mathematically simple turbulence closure model for attached and separated turbulent boundary layers. *AIAA J.* **23**, 1684–1692.

JONES, W. P. & LAUNDER, B. E. 1972 Some properties of sink-flow turbulent boundary layers. *J. Fluid Mech.* **56**, 337–351.

KONZELMANN, U. & FASEL, H. 1991 Numerical simulation of a three-dimensional wave packet in a growing flat plate boundary layer. In *Boundary Layer Transition and Control Conf., 8–12 April 1991, Cambridge.* R. Aero. Soc.

MCDONALD, H. 1968 The effect of pressure gradient on the law of the wall in turbulent flow. *J. Fluid Mech.* **35**, 311–336.

NAGANO, Y., TAGAWA, M. & TSUJI, T. 1992 Effects of adverse pressure gradients on mean flows and turbulence statistics in a boundary layer. *Eighth Symp. on Turbulent Shear Flows, Sept. 9–11, 1991, Münich.* Springer.

PATEL, V. C. 1965 Calibration of Preston tube and limitations of its use in pressure gradients. *J. Fluid Mech.* **23**, 185–208.

PERRY, A. E., HENBEST, S. & CHONG, M. S. 1986 A theoretical and experimental study of wall turbulence. *J. Fluid Mech.* **165**, 163–199.

PERRY, A. E., LIM, K. L. & HENBEST, S. M. 1987 An experimental study of the turbulence structure of smooth- and rough-wall boundary layers. *J. Fluid Mech.* **177**, 437–466.

RAI, M. M. & MOIN, P. 1991 Direct numerical simulation of transition and turbulence in a spatially evolving boundary layer. *10th CFD Conf., June 24–26 1991, Honolulu: AIAA*-91-1607.

SAMUEL, A. E. & JOUBERT, P. N. 1974 A boundary layer developing in an increasingly adverse pressure gradient. *J. Fluid Mech.* **66**, 481–505.

SCHLICHTING, H. 1979 *Boundary Layer Theory*, 7th edn. McGraw-Hill.

SCHOFIELD, W. H. 1981 Equilibrium boundary layers in moderate to strong adverse pressure gradients. *J. Fluid Mech.* **113**, 91–122.

SIMPSON, R. L., CHEW, Y. T., SHIVAPRASAD, B. G. & SHILOH, K. 1981 The structure of a separating turbulent boundary layer. *J. Fluid Mech.* **113**, 23–90.

SPALART, P. R. 1986 Numerical study of sink-flow boundary layers. *J. Fluid Mech.* **172**, 307–328.

SPALART, P. R. 1988a Direct simulation of a turbulent boundary layer up to $R_\theta = 1410$. *J. Fluid Mech.* **187**, 61–98.

SPALART, P. R. 1988b Direct numerical study of leading-edge contamination. *AGARD Symp. on Fluid Dyn. of 3D Turb. Shear Flows and Transition, Oct. 3–6 1988, Turkey.*

SPALART, P. R. & LEONARD, A. 1986 Direct numerical simulation of equilibrium turbulent boundary layers. In *Turbulent Shear Flows 5* (ed. F. J. Durst *et al.*). Springer.

SPALART, P. R., MOSER, R. D. & ROGERS, M. M. 1991 Spectral methods for the Navier–Stokes equations with one infinite and two periodic directions. *J. Comput. Phys.* **96**, 297–324.

STEWART, R. W. 1956 Irrotational motion associated with free turbulent flows. *J. Fluid Mech.* **1**, 593–606.

STREETT, C. L. & MACARAEG, M. G. 1990 Spectral multi-domain for large-scale fluid dynamic simulations. *Appl. Numer. Maths* **6**, 123–139.

WATMUFF, J. H. 1990 An experimental investigation of a low Reynolds number turbulent boundary layer subject to an adverse pressure gradient. *1989 Ann. Res. Briefs, NASA/Stanford Ctr for Turb. Res.*

WATMUFF, J. H. 1992 A high-speed cross-wire data-reduction algorithm. *Exp. Thermal Fluid Sci.* (submitted).

WATMUFF, J. H., PERRY, A. E. & CHONG, M. S. 1983 A flying hot-wire system. *Exp. Fluids* **1**, 63–71.

WATMUFF, J. H. & WESTPHAL, R. V. 1989 A turbulent boundary layer at low Reynolds number with adverse pressure gradient. *Tenth Australasian Fluid Mech. Conf., Dec. 11–15, 1989, Melbourne.*

WEI, T. & WILLMARTH, W. W. 1989 Reynolds-number effects on the structure of a turbulent channel flow. *J. Fluid Mech.* **204**, 57–95.

WOOD, D. H. & WESTPHAL, R. V. 1988 Measurements of the free-stream fluctuations above a turbulent boundary layer. *Phys. Fluids* **31**, 2834–2840.